

Crater Ice Deposits Near the South Pole of Mars

by

Owen William Westbrook

Submitted to the Department of Earth, Atmospheric, and Planetary
Sciences

in partial fulfillment of the requirements for the degree of

Master of Science in Earth and Planetary Sciences

at the

MASSACHUSETTS INSTITUTE OF TECHNOLOGY

June 2009

© Massachusetts Institute of Technology 2009. All rights reserved.

Author

.....
Department of Earth, Atmospheric, and Planetary Sciences

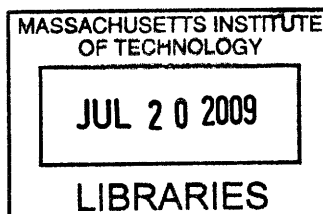
May 22, 2009

Certified by

.....
Maria T. Zuber
E. A. Griswold Professor of Geophysics
Thesis Supervisor

Accepted by

.....
Daniel Rothman
Professor of Geophysics
Department of Earth, Atmospheric and Planetary Sciences



ARCHIVES

Crater Ice Deposits Near the South Pole of Mars

by

Owen William Westbrook

Submitted to the Department of Earth, Atmospheric, and Planetary Sciences
on May 22, 2009, in partial fulfillment of the
requirements for the degree of
Master of Science in Earth and Planetary Sciences

Abstract

Layered deposits atop both Martian poles are thought to preserve a record of past climatic conditions in up to three km of water ice and dust. Just beyond the extent of these south polar layered deposits (SPLD), dozens of impact craters contain large mounds of fill material with distinct similarities to the main layered deposits. Previously identified as outliers of the main SPLD, these deposits could offer clues to the climatic history of the Martian south polar region. We extend previous studies of these features by cataloging all crater deposits found near the south pole and quantifying the physical parameters of both the deposits and their host craters. Using MOLA topography data, MOC and THEMIS imagery, and SHARAD radar sounding data, we characterize the distribution, morphology, and structure of the deposits. In addition, we examine the effect of the crater microenvironment on the formation and persistence of these deposits, exploring the relative importance of solar and eolian processes in shaping their present-day distribution and appearance. We consider the possibility that crater sand dunes may have promoted ice accumulation over time and weigh various explanations for the origins and larger climatic significance of these features.

Thesis Supervisor: Maria T. Zuber

Title: E. A. Griswold Professor of Geophysics

Acknowledgments

This thesis was made possible by NASA grants #NNG05GB65G and #NNX08AD95G and the contributions of many people. The project grew out of initial investigations done by Shane Byrne (LPL, U. of Arizona), who continued to provide expert feedback throughout the research process. Oded Aharonson (Caltech) helped format the MOLA polar dataset used in this study, Roger Phillips and Than Putzig (SWRI) provided access to and instruction on SHARAD data, Jack Holt and Prateek Choudhary (UT-Austin) produced the necessary SHARAD clutter simulations, and Anthony Egan (SWRI) performed depth-correction of the SHARAD radargrams. Linda Meinke, Daniel Sheehan, and Alex Evans (MIT) also lent technical assistance. Above all, many thanks to Maria Zuber for her invaluable hours of guidance in advising this project.

Contents

1	Introduction	9
2	Data and Methods	11
2.1	Datasets	11
2.2	Deposit Identification, Classification, and Characterization	12
2.3	Measurement Techniques	13
2.3.1	Measurement of Deposit Parameters	13
2.3.2	Radar Sounding	14
2.3.3	Insolation Measurements	15
3	Results	19
3.1	Deposit Identification, Characterization, and Morphology	19
3.1.1	Layering and Internal Structure	19
3.1.2	Flow Features	24
3.1.3	Ridges	24
3.1.4	Stacked Deposits	26
3.1.5	Dune Fields	28
3.1.6	Albedo Patterns	28
3.2	Deposit Distribution and Physical Parameters	28
3.2.1	Geographic Distribution	29
3.2.2	Geological Setting	29
3.2.3	Deposit Age	33

3.3	Crater Insolation	34
4	Discussion	39
4.1	Deposit Composition	39
4.2	Deposit Morphology	40
4.3	The Polar Crater Micro-environment	42
4.3.1	Solar Insolation	43
4.3.2	Crater Winds, Eolian Sediment Transport, and Atmospheric Conditions	45
4.3.3	Crater Dune Fields and Seasonal Frost	47
4.4	Deposit Origin and Evolution	50
5	Conclusions	53

Chapter 1

Introduction

The Martian poles are covered by layered deposits of water ice and dust stacked up to three km thick. Representing tens of millions of years of accumulation at the south pole, these polar layered deposits are thought to reflect changes in the Martian climate in the recent geologic past. Just beyond the south polar layered deposits (SPLD) lie dozens of craters containing large mounds of fill material of uncertain origin and composition (Figure 3-1). Many of these crater-filling deposits (CFDs) exhibit layering in orbital images, and some have previously been mapped as outliers of the main SPLD (Tanaka & Scott, 1987; Tanaka & Kolb, 2001). These deposits have been examined previously for evidence of flow and fracture (Byrne, 2003) and general morphological and geographic trends (Russell et al., 2004; Russell & Head, 2005). In addition, Russell et al. (2004) performed energy balance modeling on a hypothetical polar crater filled with ice and were able to reproduce some of the morphological features seen in these deposits.

Here, we extend this earlier work by cataloging and quantifying the physical parameters of all detectable examples of these CFDs found in the south circumpolar region. Further, we investigate the relative roles of various mass-balance processes, particularly solar flux and crater wind conditions, in controlling the surface morphologies of these deposits. No single modification process can easily explain the observed distribution and morphologies of these deposits, suggesting that these CFDs are the expression of multiple modification

forces and formation processes. While these deposits share many of the features of the polar layered deposits, their isolation from the main SPLD points to the polar crater micro-environment as the explanation for their existence and persistence. In addition to the unique insolation, wind, and atmospheric conditions found inside these craters, their ability to trap windblown sediments suggests that CFDs may originate from the buildup of icy deposits upon a substrate of sand dunes and dust. From the observed morphological evidence, we develop a theory for the formation and preservation of these features and their connection to Martian climate.

Chapter 2

Data and Methods

2.1 Datasets

Much of the analysis for this project was performed on a 100 pixel per degree (ppd) Mars Orbital Laser Altimeter (MOLA) (Zuber et al., 1992; Smith et al., 2001) digital elevation model (DEM) of the Martian south polar region in polar stereographic projection, a dataset extending from roughly 55° S to the pole.¹ Georeferencing was performed using the transformations provided by the Planetary Data System.² Additional polar datasets at resolutions of 128, 256, and 512 ppd were used as well.

For deposit identification and morphology, MOLA polar shaded relief maps (Neumann et al., 2001) were employed along with mosaics of Mars Orbiter Camera (MOC) images (Malin & Edgett, 2001) and Thermal Emission Imaging System (THEMIS) infrared images (Christensen et al., 2004).³ Finally, processed radargrams from the SHallow RADar (SHARAD) instrument (Seu et al., 2007) aboard the Mars Reconnaissance Orbiter (MRO) were examined to investigate deposit structure, subsurface layering, and composition.

¹Formatted courtesy of Oded Aharonson of the California Institute of Technology

²http://pds-geosciences.wustl.edu/geo/mgs-m-mola-5-megdr-l3-v1/mgsl300x/catalog/dsmap_polar.cat

³Presented by <http://www.google.com/mars>

2.2 Deposit Identification, Classification, and Characterization

The first step in our analysis was to catalog all detectable instances of the deposits and classify them based on morphological criteria. CFD identification was performed primarily on the basis of MOLA topography data, as well as MOC imagery and THEMIS infrared data. The typical south polar crater-filling mound has a characteristic shape with a smooth, flattened top and a clearly-defined, continuous boundary with a distinct bounding slope that is steepest at the deposit edges. In some cases, a bounding ridge completely or partially encircles the flat top of the deposit (Figure 3-2). This set of morphological traits contrasts with those of impact crater topography such as central peaks, which exhibit gradually steepening boundary slopes and peak-like aspects (Melosh, 1989). In addition, CFDs are commonly irregularly shaped and offset from crater center. Many deposits also exhibit layering at their margins in MOLA, MOC, or THEMIS data. Unlike topographic features generated during the impact cratering process, such as central peaks, CFDs are commonly irregularly shaped and offset from crater center. Using mapping by Byrne (2003) as a starting point, we examined any prominent raised areas of topography on the floors of craters within roughly 30° of the pole for these characteristics.

After tentatively confirming a deposit as a secondary feature with possible ice content, additional morphological information was collected. Among the data recorded were the presence and number of any layers, ridges within the deposits, or other features consistent with glacial flow. The geologic context of each deposit and its host crater was identified according to regional mapping by Scott & Carr (1978) and Tanaka & Scott (1987). Sand dunes atop the deposits or elsewhere in the crater were also noted. Dunes are prevalent in craters in the southern hemisphere, detectable by their wavy dune forms, low albedo in MOC images, and high albedo in THEMIS infrared images. A possible link between these dunes and CFDs will be discussed later.

2.3 Measurement Techniques

2.3.1 Measurement of Deposit Parameters

In order to constrain our theories for the formation and evolution of these CFDs and assist in future modeling efforts, we compiled comprehensive measurements of the physical properties of the deposits and their host craters. To do so, we adapted techniques developed by Watters & Zuber (in preparation) for the automated detection of quasi-circular depressions (QCDs) in the northern lowlands of Mars. The detection algorithm operates by fitting circles to closed contours in MOLA topography data and then using a Euclidean-distance cluster analysis to identify sets of fitted circle centers. This method proves effective in identifying and measuring craters in MOLA DEMs as long as the crater rims have not been significantly degraded by erosion or embayment.

The detection routine was run on the 100 ppd MOLA DEM of the south polar region, a dataset in polar stereographic projection with a nominal resolution of 589.26 m/pixel. Running the algorithm on the entire south polar region would have required a prohibitive amount of computing power, so the data were divided into 800 x 800 pixel-wide parcels, each overlapping by 100 pixels. The detection program was run only on those parcels which had previously been identified as having craters containing CFDs.

For each parcel, 20 contour levels are calculated, and all closed contours within a certain minimum and maximum length are fit with circles. Cluster analysis identifies groupings of circle centers, and for each grouping, a mean circle center is calculated. Next, eight transects running through the calculated center are interpolated onto the DEM every $\pi/4$ radians. In each of these transects, the maximum points on either side of the crater center are interpreted as the crater rim and the minimum points as the bottom of the crater floor. Combining measurements from each transect, the crater diameter is computed as the average distance between points on the rim, the crater depth as the average height between the crater rim and the crater floor, and the crater center as the mean halfway point between the rim in each profile.

For every crater detected in the MOLA data with our routine, we recorded the following parameters along with measurement errors where appropriate: latitude and longitude of the crater center, crater diameter, depth, rim elevation, and aspect ratio (depth to diameter). If a deposit was present in the crater, we also noted the latitude, longitude, and elevation of the peak of that deposit. The CFD peak was defined as the maximum elevation within the crater walls. First, the maximum elevation within 40% of the crater’s radius from crater center was calculated. From there, we computed the maximum height within a 5x5 pixel square centered on the previously calculated maximum, iterating this process until the highest point on the deposit was reached. All peak identifications were checked manually to ensure that the routine did not mistake a point on a crater’s walls or a local maximum within the deposit for the actual CFD peak. False detections were thrown out and rerun manually. We also recorded the offset between the crater center and CFD peak, both in m and normalized by the crater radius.

2.3.2 Radar Sounding

The SHARAD sounding radar provides a means of probing the Martian subsurface and investigating the internal structure of these CFDs. The instrument emits a nominal 10 W, 85 μs chirped pulse with a 20-MHz center frequency with a 10-MHz bandwidth, and this signal has cross-track and along-track footprints of 3–6 km and 0.3–1 km, respectively, on the Martian surface. Once a radar signal is transmitted to the surface, reflections may occur both from the surface and from dielectric interfaces within the subsurface. SHARAD is able to detect interfaces hundreds of meters deep at vertical resolutions of 15 m in free space and $15/\epsilon$ m in material of relative permittivity ϵ (Seu et al., 2007).

With the assistance of the SHARAD science team, SHARAD observations crossing craters of interest were examined for evidence of internal layering in the deposits. For these evaluations, only observations using the Doppler focused processor were used (see Seu et al. (2007) for further details about the processing scheme). For cases where focused processor observations had not been archived, the focusing was performed using the science team’s

default processor settings.

The main challenge in the interpretation of radar data is distinguishing subsurface returns from off-nadir surface reflections. These extraneous returns, known as "surface clutter," were predicted for radargrams of interest on the basis of MOLA topography using a facet-based model (Holt et al., 2008).⁴

The final step in analysis of the radar data was conversion of the radargrams from time-delay space to depth (m).⁵ A dielectric constant of 3.15 was assumed, corresponding to water ice with a dust content of a few percent, as indicated by previous studies of the SPLD (Plaut et al., 2007; Zuber et al., 2007).

2.3.3 Insolation Measurements

The prevalence of these deposits near the north and south poles and the trend of increasing crater fill at higher latitudes suggest that solar insolation plays a role in controlling the distribution and morphology of the deposits. For some of the more prominent deposits, we calculated the solar flux in and surrounding the host crater, both accounting for and ignoring the effects of shadowing. Our primary object was to determine whether any correlation exists between current insolation patterns and the observed shapes of the CFDs, and therefore our insolation calculations do not include the effects of scattering and absorption by the Martian atmosphere, reradiation off of the crater walls, or heat conduction within the crater or the deposit. Any detailed energy balance model of these deposits, such as that developed by Russell et al. (2004), would have to address these effects.

Insolation analyses were run on 75-200 pixel wide subregions of the 100 ppd MOLA DEM of the south polar region. From the DEM, we calculate the slope and aspect of every grid point, with aspect angles measured counterclockwise from north. Ephemeris data and Mars orbital parameters are then used to find the solar hour angle, hr , and declination, dec , for a given ephemeris time and longitude. At a given latitude, the solar altitude, alt_s , and azimuth,

⁴Clutter simulations performed courtesy of Jack Holt and Prateek Choudhary of the University of Texas-Austin

⁵Depth correction carried out courtesy of Anthony Egan of the Southwest Research Institute

az, for a flat surface are given by

$$\sin(alt_s) = \sin(lat) * \sin(dec) + \cos(lat) * \cos(dec) * \cos(hr) \quad (2.1)$$

$$\cos(az) = \frac{\sin(dec) - \sin(lat) * \sin(alt_s)}{\cos(lat) * \cos(alt_s)} \quad (2.2)$$

$$(2.3)$$

For a non-horizontal surface with a given slope, s , and aspect, a , the solar altitude, alt_{ss} , is calculated as

$$\sin(alt_{ss}) = \sin(alt_s) * \cos(s) + \cos(alt_s) * \sin(s) * \cos(a - az) \quad (2.4)$$

$$(2.5)$$

For the cases in which we accounted for shadowing, we also calculate the altitude of the horizon and compare that value with the solar altitude. First, at the solar azimuth angle computed previously, we interpolate a rhumb line track⁶ of length 200 km onto the DEM, producing a profile of the terrain in the direction of the sun. This profile, $elev$ must be corrected for planetary curvature by a factor of h_c , where

$$h_c = \frac{R_m}{\cos(d/R_m)} - R_m \quad (2.6)$$

$$elev_c = elev - h_c \quad (2.7)$$

Here, R_m is the radius of Mars in the MOLA projection and d is the distance from the point on the DEM to the interpolated point on the curvature-corrected rhumb line profile, $elev_c$. After this correction is applied, the altitude of each point on the rhumb line, alt_{rhumb} is calculated as

$$\tan(alt_{rhumb}) = \frac{elev_c}{d} \quad (2.8)$$

$$(2.9)$$

⁶A rhumb line is a path of constant bearing; thus, it crosses all lines of longitude at the same angle.

The horizon angle is the maximum altitude along the rhumb line track for each point on the surface. If the horizon angle anywhere along this track is greater than the solar altitude, then the sun is below the horizon and the solar flux incident on that grid point is zero. For simplification, the sun was considered to be a point source. Because of the computational demands of the shadowing calculations, the full shadowing analysis was only run on a subset of the craters whose insolation patterns were studied in detail.

The above procedure produces a map of flux values, in W/m^2 , incident on the top of the Martian atmosphere for a specific time in Mars' orbit. To calculate the average annual insolation, we first found the average daily insolation for 30 days spaced evenly in time throughout one Mars orbit. For each day, insolation was calculated at 24 equally spaced times. These 24 measurements were averaged to yield a mean daily value, and the 30 mean daily values were averaged to produce a mean yearly insolation map. Increasing the frequency of sampling of the insolation values both within a day and within a year did not noticeably alter the results.

Chapter 3

Results

3.1 Deposit Identification, Characterization, and Morphology

Using the criteria described above, 75 craters were identified as containing secondary fill deposits with potential ice content (Figure 3-1). This count includes a small number of marginal cases. Our initial mapping of the distribution of CFDs revealed a number of morphological features suggestive of the processes at work in shaping the deposits. Many of these characteristics have been previously commented on by others (Byrne, 2003; Russell et al., 2004; Russell & Head, 2005), but their interpretation is by no means settled. A summary of the morphology types found in each deposit is given in Table 3.1.

3.1.1 Layering and Internal Structure

While the prototypical examples of these CFDs do exhibit layering, we found many mounded deposits without layering evident in either regional-scale MOC or THEMIS imagery. Of the 75 deposits identified in this work, 35 of them had noticeable layering in THEMIS data, and 18 of these had strata visible in wide-angle MOC images. Only 6 deposits contained layers that were visible in MOLA shaded relief maps.

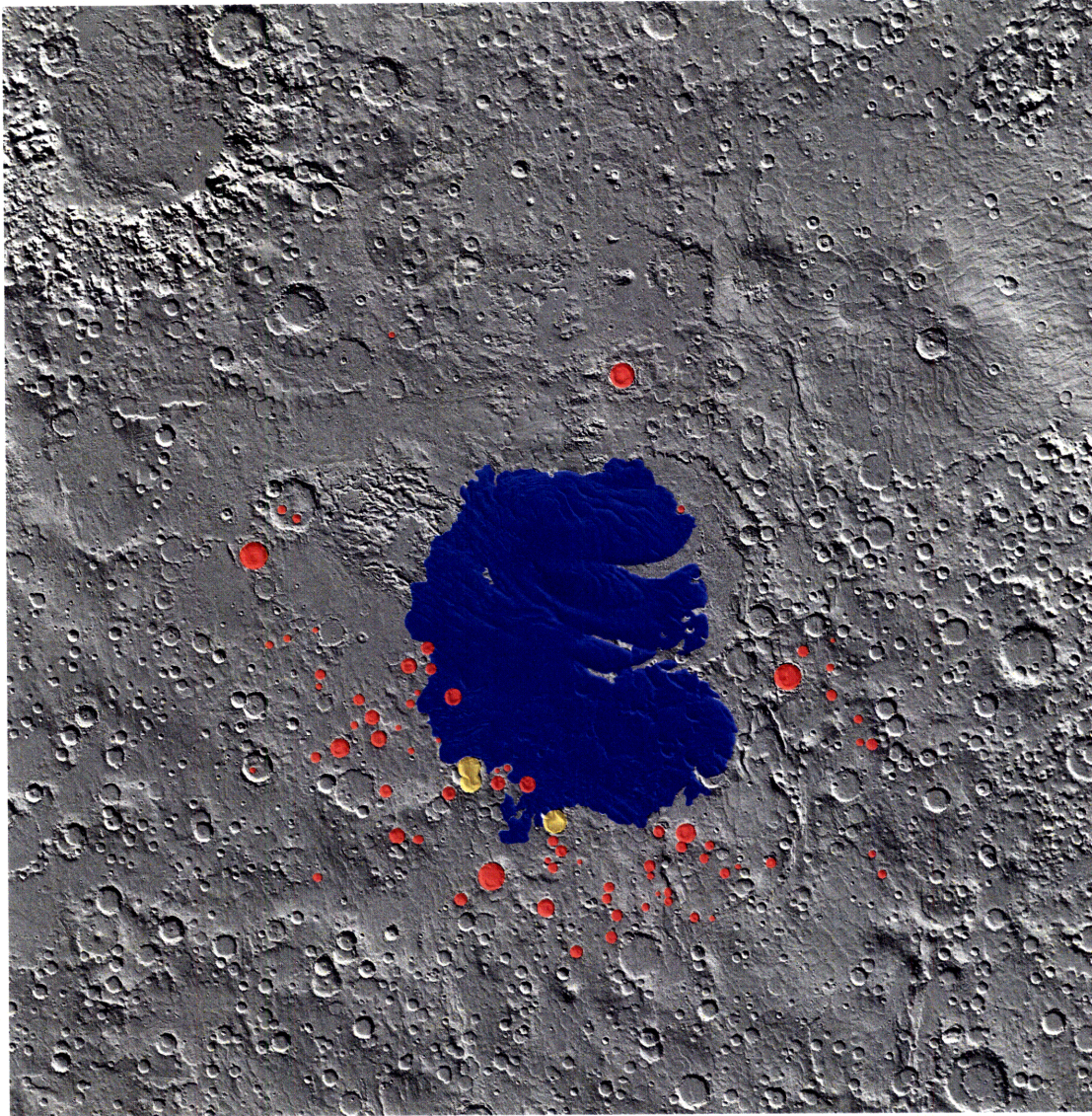


Figure 3-1: MOLA relief map shaded from the upper right of the south polar region. Craters containing deposits measured in this work are shaded red; craters shaded yellow hold deposits that could not be automatically measured because of the non-circularity of the host craters. The approximate extent of the SPLD as mapped by Kolb & Tanaka (2001) is shown in blue.

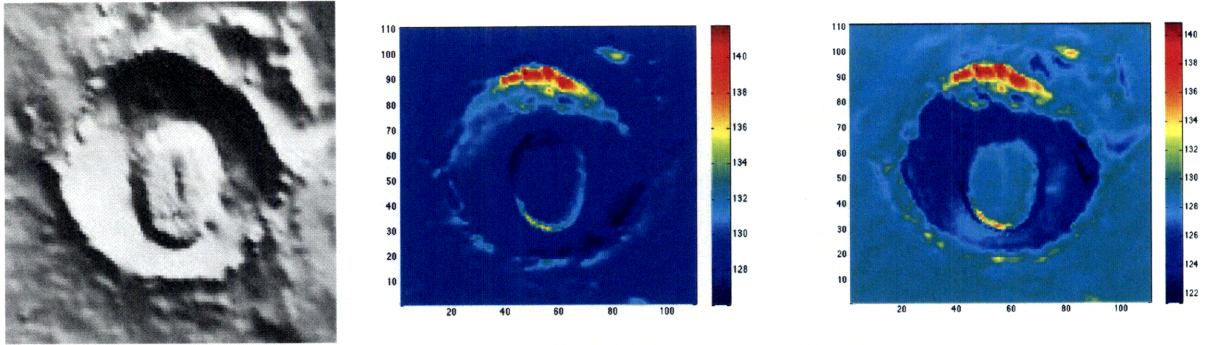


Figure 3-2: *L to R* : MOLA shaded relief, average annual insolation levels with full shadowing analysis, and average annual insolation levels without consideration of shadowing for a 35 km diameter crater at 71.2° S, 158.7° E. This deposit illustrates many of the morphological traits common to CFDs: a mounded aspect, flattened top, and steep bounding slope. A dune field is also present atop the deposit. Insolation scale is in W/m^2 .

SHARAD radargrams provide a valuable complement to surface data for probing the internal characteristics of these deposits. Because of the challenge surface clutter poses to radar interpretation, we only used SHARAD to examine the largest CFDs. The radargrams of one deposit in particular, in Burroughs Crater, revealed up to half a dozen well-defined, flat-lying, subsurface layers (Figure 3-3). These layers were not visible in clutter simulations, implying that they are real features. An unnamed crater just outside the SPLD, at 79.9° S, -126.0° E, also exhibits internal layering, but this layering is tilted to roughly the same angle as the surface slope of the deposit (Figure 3-4). Layering is also strongly apparent in radargrams crossing a large mounded deposit in Korolev Crater, in the north polar region, that appears to be analogous to those in the southern hemisphere.

Several other large deposits, including those in South, Playfair, and Richardson Craters, exhibited volumetric scattering in their radar returns even though well-defined layers were not visible (Figure 3-5). This volumetric scattering, the result of inhomogeneities within the subsurface, is present only in the radar returns originating from directly within the deposits and is not seen in the surrounding, ice-free areas. Radargrams with similar characteristics are seen throughout the SPLD where layering is otherwise indistinct or not apparent, reinforcing the connection between these deposits and the main SPLD.

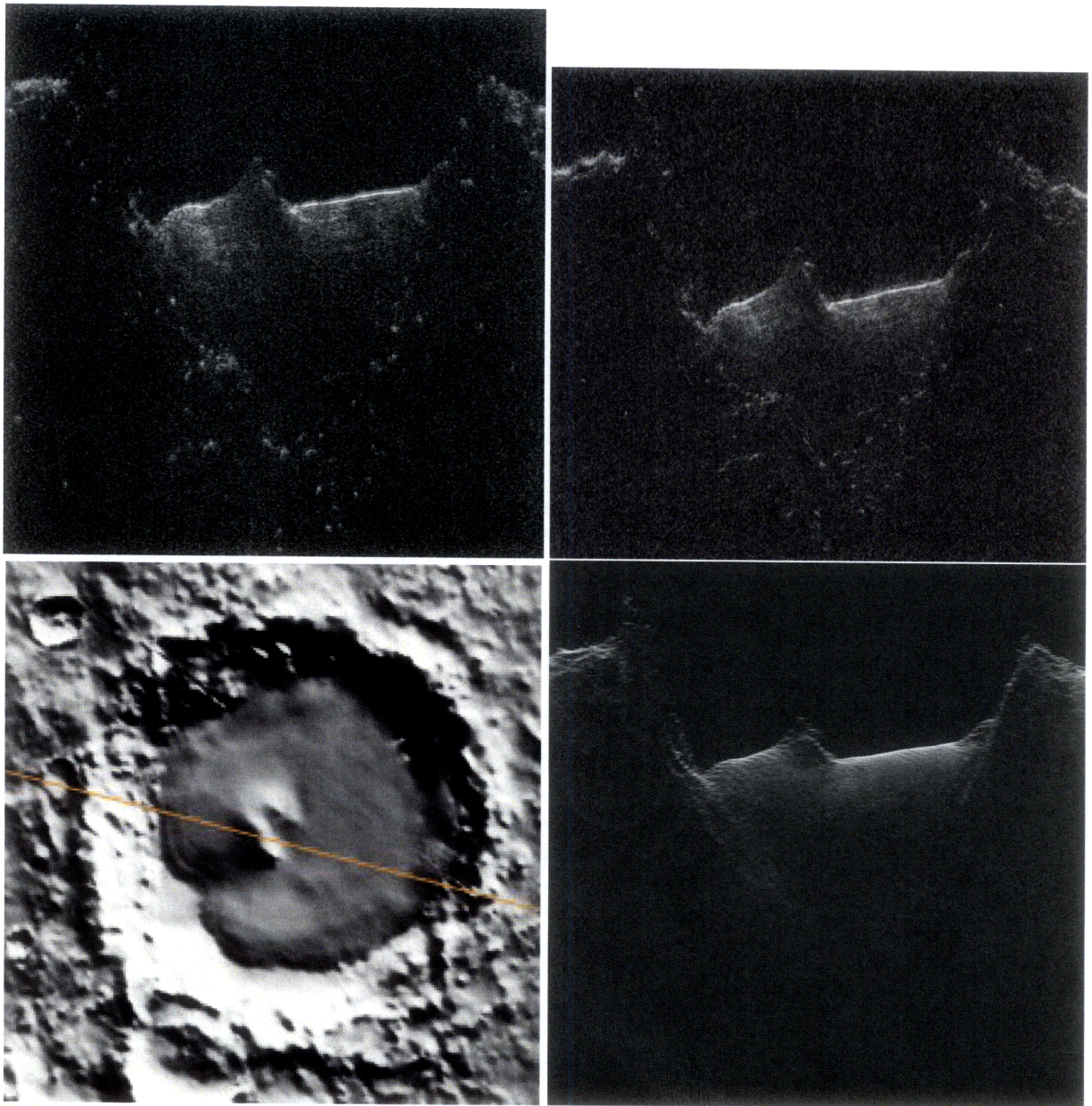


Figure 3-3: *Clockwise from top left* : SHARAD radargram (vertical axis: time delay), SHARAD depth-corrected radargram (vertical axis: distance), surface clutter simulation, and MOLA shaded relief map for Burroughs Crater (72.2° S, 117° E). Faint layering is visible in the radargram that is not present in the clutter simulation. This layering can also be seen at the edges of the deposit in the MOLA shaded relief map.

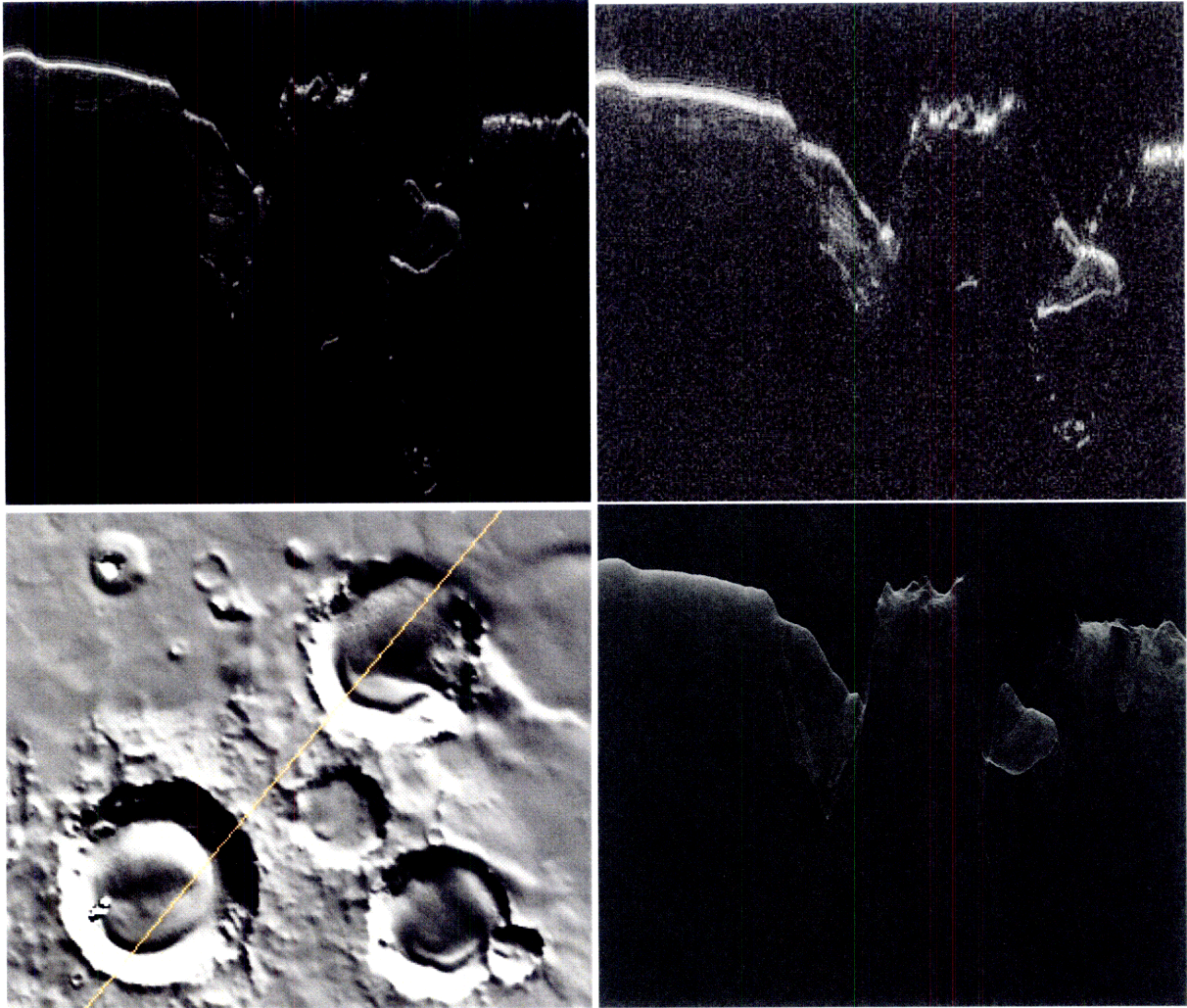


Figure 3-4: *Clockwise from top left* : SHARAD radargram (vertical axis: time delay), SHARAD depth-corrected radargram (vertical axis: distance), surface clutter simulation, and MOLA shaded relief map for an unnamed crater, at 79.9° S, -125.0° E, and Playfair Crater, at 78.3° S, -126.0° E. Playfair is the crater in the bottom left of the MOLA shaded relief map and the rightmost crater in the radar data. Layering is evident in both the main body of the SPLD and in the fill deposit in the unnamed crater adjacent to the SPLD, though no layering is seen in a similar deposit within Playfair Crater.

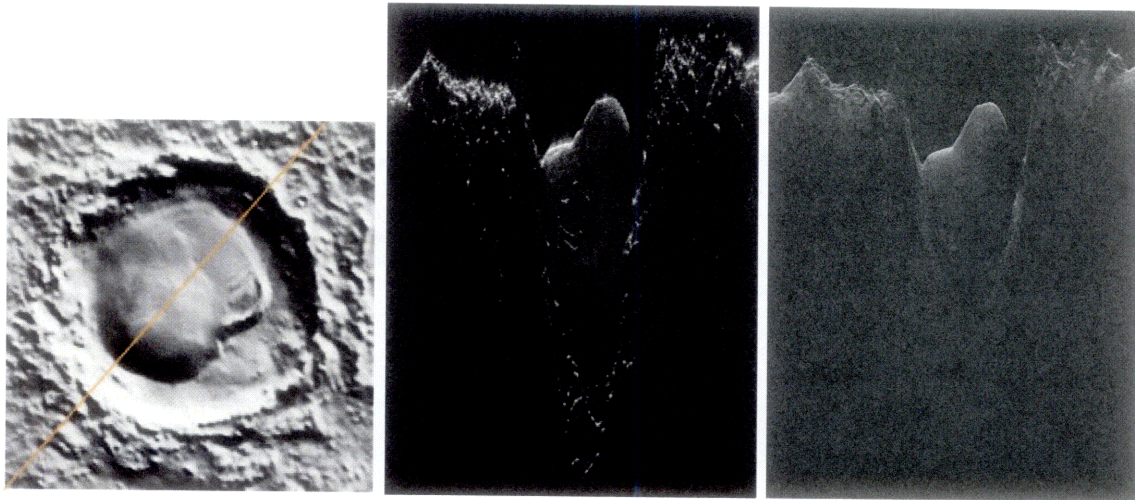


Figure 3-5: *L to R* : MOLA shaded relief map, SHARAD radargram (vertical axis: time delay), and surface clutter simulation for South Crater (72.2 °S, 117 °E). Layering is not apparent within the deposit, but the radar return from within the deposit does exhibit the fuzzy, volumetric scattering characteristic of the SPLD. This characteristic is not seen in returns originating from outside the deposit.

3.1.2 Flow Features

A handful of craters adjacent to or in contact with the main SPLD exhibit morphology consistent with the viscous flow of material. In particular, Reynolds Crater (Figure 3-6) at 75° S, 202.1° E, and Richardson Crater (Figure 3-7) at 72.4° S, 179.6° E, are two multiple crater sites where fill material appears to have flowed from one crater into another. Directly north of Richardson Crater, a tongue of fill material extends between two other craters where their shared rims have eroded, though both craters are relatively empty of fill. Flow characteristics can also be seen in single craters, such as the unnamed one at 78.9° S, -143.5° E (Figure 3-8), where the morphology suggests an inflow of icy material spilling into the crater from the main SPLD.

3.1.3 Ridges

Other features highly suggestive of viscous flow are the edge ridges seen in CFDs where the fill material is close to or in contact with the crater walls. A total of 10 deposits exhibited such

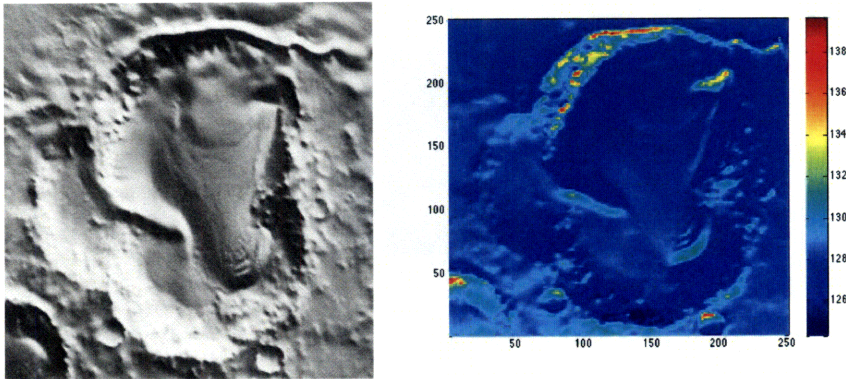


Figure 3-6: *Left* : MOLA relief map illuminated from the upper right of Reynolds Crater, at 75° S, 202.1° E, which contains mounded crater fill with a morphology consistent with the flow of glacial material away from the south pole and the main SPLD. Ridges are visible on the lower (northernmost) end of the lobe, possibly the result of compression of the icy fill mass against the crater wall. *Right* : Average annual insolation levels in Reynolds Crater (without shadowing). The equatorward-facing slopes of the edge ridges receive significantly more insolation than the poleward-facing slopes. Insolation scale is in W/m^2 .

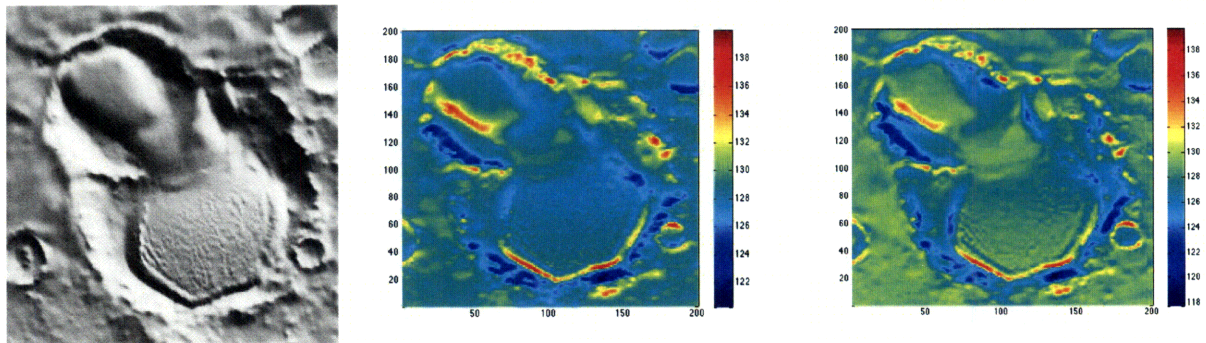


Figure 3-7: *Left* : MOLA relief map illuminated from the upper right of Richardson Crater, at 72.4° S, 179.6° E. This crater, bordering the main SPLD, appears to contain material which has flowed from the upper left subcrater into the main crater. Dunes are visible on the surface of the larger deposit lobe, as is a bounding ridge. Average annual insolation levels with (*right*) and without (*center*) consideration of the effects of shadowing are also shown. Scale is in W/m^2 .

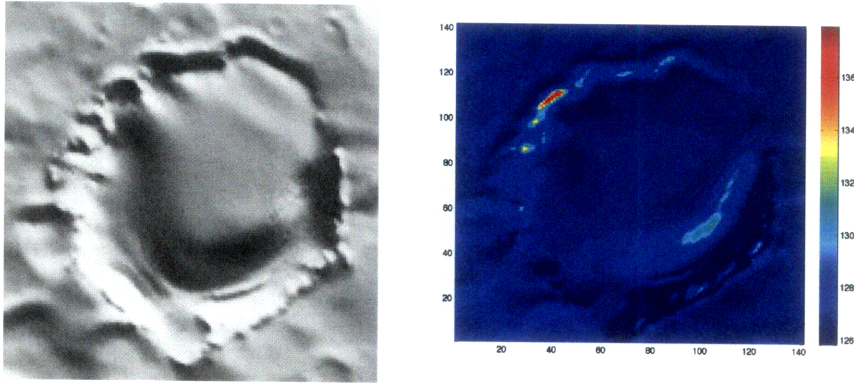


Figure 3-8: *Left* : MOLA relief map shaded from the upper right of an unnamed crater 55 km in diameter, at 78.9° S, -143.5° E. This deposit is morphologically suggestive of material flowing from the adjacent SPLD into the crater. *Right* : Average annual insolation levels without shadowing are shown in W/m².

ridges, primarily those also showing other morphological signs of viscous flow. Apparent most notably in Reynolds Crater and South Crater (Figure 3-9), these ridges could form from compression as the icy mass encountered the crater walls (Byrne, 2003). Taking DEM transects perpendicular to the ridges, we found average ridge spacings of 3.15 ± 0.85 km for the 7-8 ridges in the South Crater CFD and average spacings of 2.76 ± 0.72 km for the 6-7 ridges in the Reynolds Crater CFD. For both deposits, the number of ridges detected varied slightly depending on the positioning of the transects.

3.1.4 Stacked Deposits

A few craters, most located just off the edge of the SPLD, contain deposits that appear to consist of multiple superposed mounds. In these cases, the lowest mound has a relatively flat profile and any overlying mounds exhibit a more rounded form (Figures 3-9 and 3-10). In both of these instances, the upper mounds have a noticeably higher albedo in MOC images than do the lower ones.

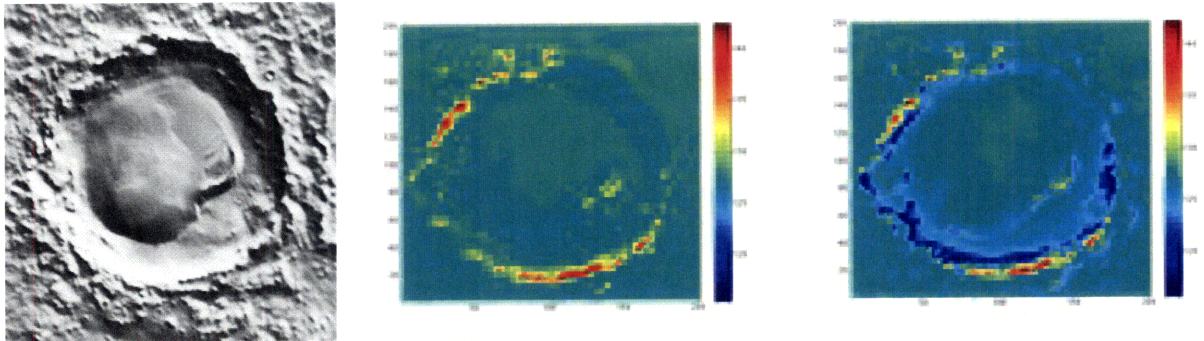


Figure 3-9: *Left* : MOLA relief map illuminated from the upper right of South Crater, at 77° S, 22° E. This 107 km diameter crater is one of the few between 270° E and 90° E containing a substantial deposit. The deposit appears to consist of stacked mounds, perhaps indicating multiple episodes of accumulation. A series of ridges is visible on the right side of the deposit with an especially prominent large bounding ridge. Average annual insolation levels with (*right*) and without (*center*) consideration of the effects of shadowing are also shown, and illustrate that the equatorward-facing ridges within the deposit receive significantly more insolation than the pole-facing slopes. Scale is in W/m^2 .

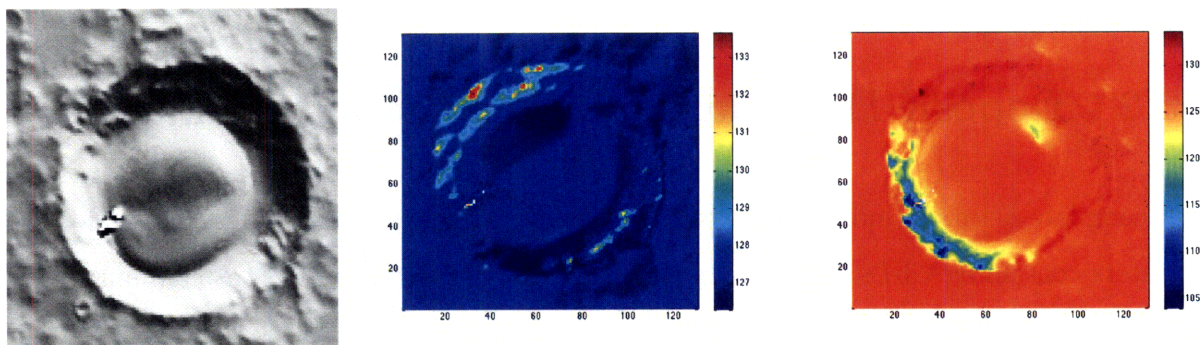


Figure 3-10: *Left* : MOLA relief map illuminated from the upper right of Playfair Crater, at 78.3° S, -126.0° E. This 64 km diameter crater appears to contain a CFD comprised of superposed mounds, perhaps indicating multiple episodes of accumulation. Average annual insolation levels with (*right*) and without (*center*) consideration of the effects of shadowing are also shown. Scale is in W/m^2 .

3.1.5 Dune Fields

A significant number of CFDs, at least 17, are also closely associated with sand dune fields. In the case of the Richardson Crater deposit and others, these dune fields lie atop and at the sides of the CFD mound (Figure 4-1). As will be discussed later, these dunes and their sand content could be connected with the formation and evolution of CFDs.

3.1.6 Albedo Patterns

A number of the deposits exhibited distinct albedo signatures that allowed them to be differentiated from the surrounding terrain and from impact crater morphology. Out of the 75 identified deposits, 64 were noticeably darker than the surrounding terrain in MOC images. Of these 64, 42 were also brighter in THEMIS infrared images to a greater degree than could be accounted for by solar incidence angle. Only 7 deposits were neither IR-bright nor dark at visible wavelengths, though these included some of the largest fill deposits, found closest to the main SPLD.

3.2 Deposit Distribution and Physical Parameters

A complete listing of individual, mean, and median crater and deposit properties for those craters containing CFDs can be found in Table 3.1. Craters identified as containing CFDs had average and median diameters of 45.1 ± 2.5 km and 42.5 ± 3.1 km, respectively. The mean and median aspect ratios (depth/diameter) for these craters were 0.027 ± 0.001 and 0.025 ± 0.002 , respectively.¹ These measured aspect ratios may be lower than typical Martian craters because the deepest point in the original crater was often covered with the raised mound of a CFD.

¹These statistics exclude the irregularly shaped Richardson and Reynolds Craters

3.2.1 Geographic Distribution

While CFDs are present near both Martian poles, only a handful of examples exist in the northern hemisphere. For that reason, this study focuses on the deposits found near the south pole of Mars and does not examine the northern examples in detail. The geographic distribution of these crater deposits provides an important modeling constraint. Measured crater deposits lie overwhelmingly between 65° S and 80° S latitude within roughly 500 km of the SPLD (Figure 3-11). In general, as noted by Russell et al. (2004) and Russell & Head (2005), deposits in closer proximity to the main SPLD tend to be more circular, less asymmetric, and fill a greater percentage of the crater's volume. Features consistent with flow also become less apparent with distance from the SPLD.

The distribution of CFDs shows a strong longitudinal bias, with the vast majority of examples lying between 150° – 240° E (Figure 3-12). This bias reflects a similar asymmetry in the SPLD, which extends much farther north between 90° – 270° E than in the opposite hemisphere.

Geographic trends are present but less evident in the placement of the deposits within their host craters. The offsets of the CFD peak from crater center, when normalized by the crater's center-to-rim radius, show no obvious trends with latitude or longitude. When these offsets are broken down into North/South and East/West components, 42 out of 73 measured deposits show an offset to the south of crater center (poleward), and 49 out of 73 show a westward offset (Figures 3-13–3-15).

We also searched for a correlation between the CFD offsets and the aspect ratios of the craters (Figures 3-16 and 3-17). In CFD-containing craters of low aspect ratio, no clear pattern in the direction or magnitude of the deposit offset is noticeable. At high aspect ratios (>0.04), however, almost all CFDs are offset westward and southward.

3.2.2 Geological Setting

The longitudinal distribution of the CFDs also appears to reflect the locations of craters in the southern circumpolar regions. Of the 75 deposits identified, 66 lie in craters mapped

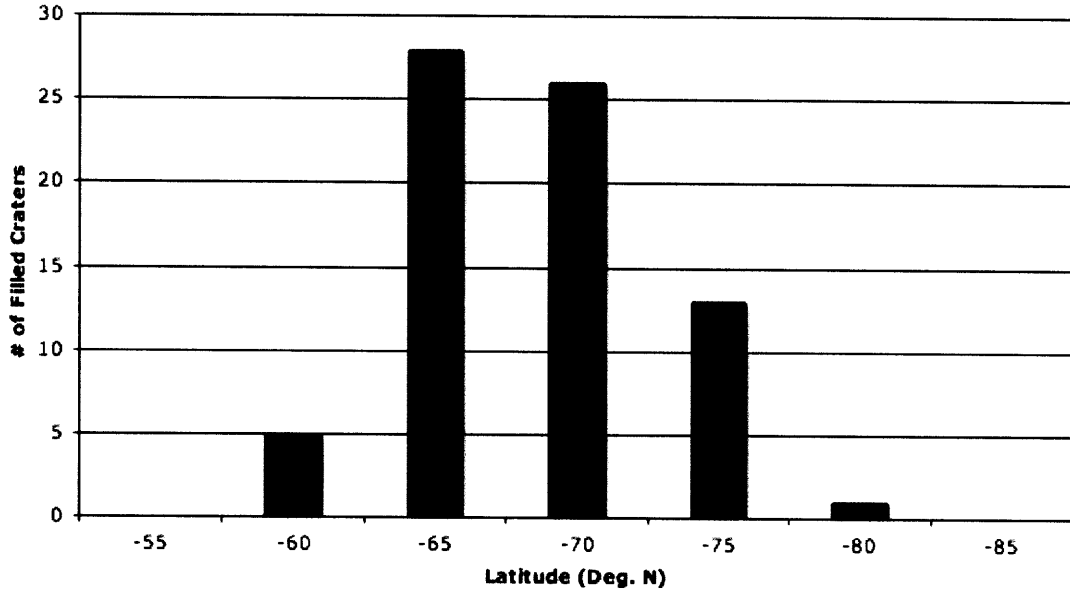


Figure 3-11: Histogram of the latitudinal distribution of CFDs measured with our automated methods. Latitude bins are 5° wide and x-axis values indicate lower latitude bounds. Observed CFDs lie concentrated between latitudes 60°–80° S.

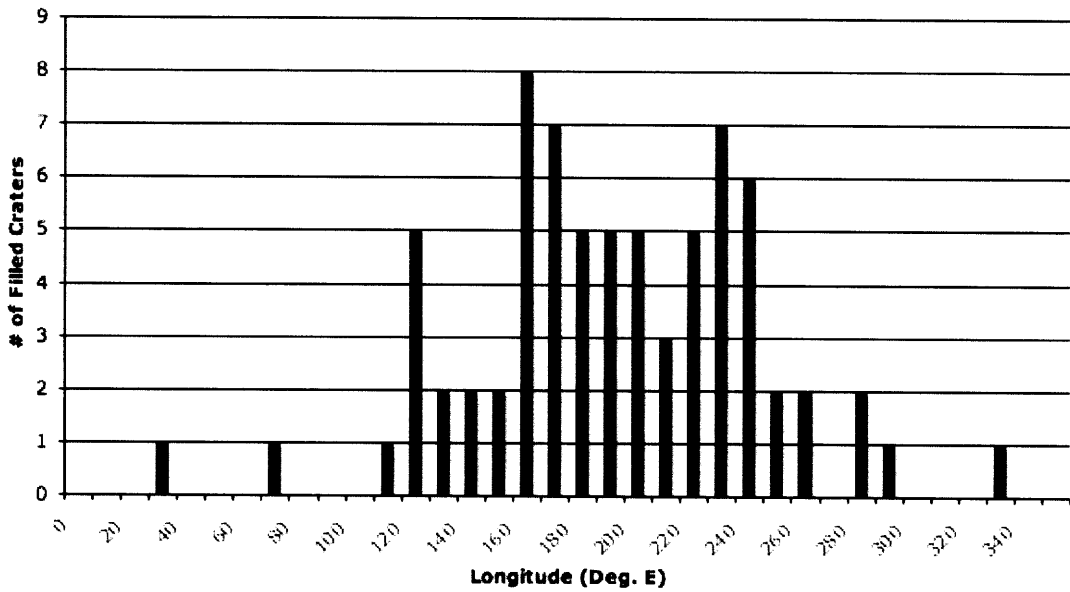


Figure 3-12: Histogram of the longitudinal distribution of CFDs measured with our automated methods. Longitude bins are 10° wide and x-axis values indicate lower longitude bounds.

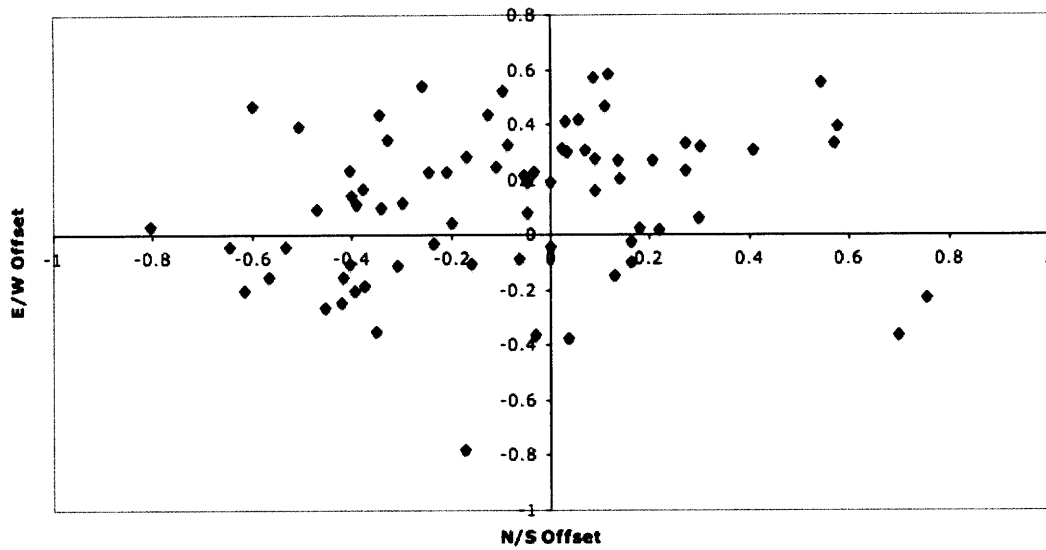


Figure 3-13: The offsets of the peak of the CFD from crater center, normalized by crater radius. Northward and westward offsets are positive; southward and eastward offsets are negative.

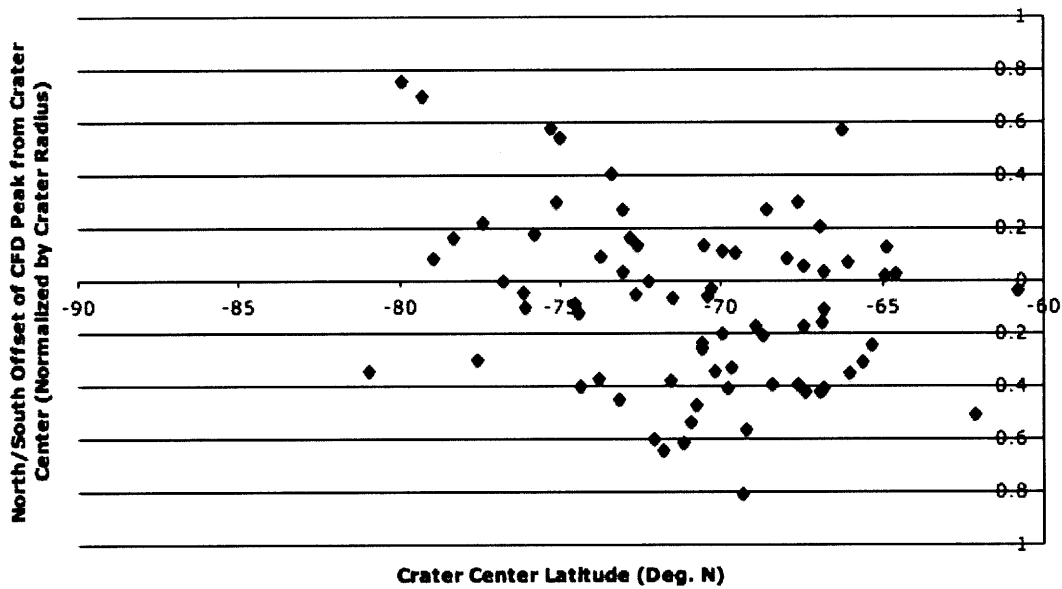


Figure 3-14: North/south offsets of CFD peaks from crater center, normalized by crater radius. Northward offsets are positive, while a negative value denotes a southward offset. A majority of the CFD peaks exhibit a northward offset, consistent with solar ablation of the equator-facing edge of the deposit.

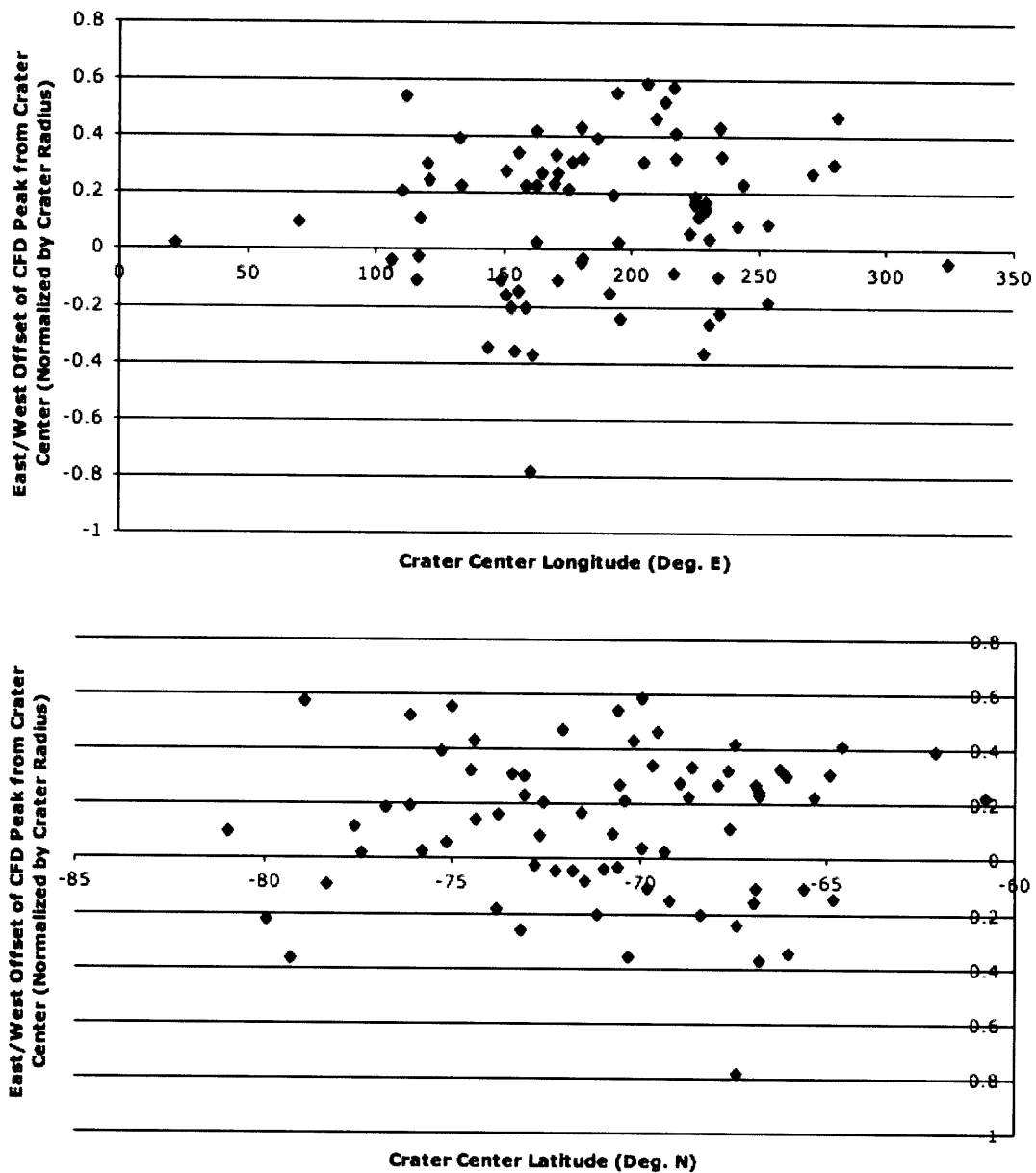


Figure 3-15: East/west offsets of CFD peaks from crater center, normalized by crater radius, plotted against crater center longitude (*top*) and latitude (*bottom*). Westward offsets are positive; eastward offsets are negative. A majority of CFD peaks display a westward displacement, consistent with Coriolis deflection for the southern hemisphere of Mars.

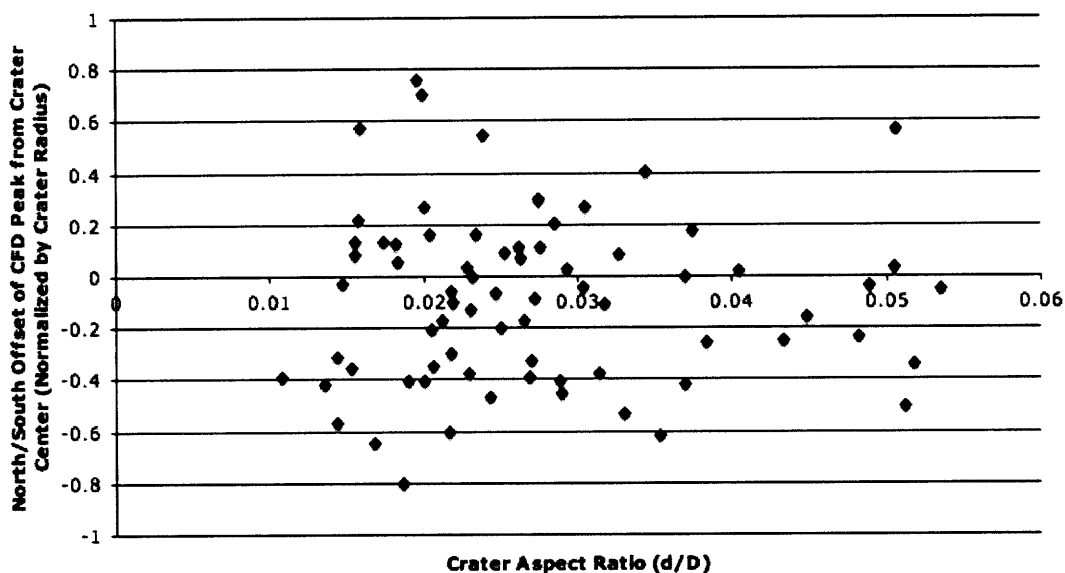


Figure 3-16: North/south offsets of CFD peaks from crater center, normalized by crater radius, plotted against the crater aspect ratio (d/D). A positive value indicates a northward offset; a negative value a southward offset. No clear pattern is evident at low aspect ratios, but the deepest craters (high d/D) tend to exhibit southward CFD offsets.

as Noachian hilly and cratered terrain (Nhc) by Scott & Carr (1978) (Table 3.1). The Nhc unit, one of the oldest and most heavily cratered on the planet, is most extensive at the same longitudes where CFDs are found. Elsewhere, much of the south polar region's terrain is covered by younger plains units that in many cases have mantled or buried preexisting craters. The remnant craters at these longitudes are therefore generally shallower in profile. One prominent exception is South Crater, at 77° S, 22° E. A relatively deep and undegraded crater, South Crater contains one of the largest CFD examples, suggesting that the lack of suitable craters is the chief reason for the longitudinal bias in CFD distribution.

3.2.3 Deposit Age

Although the CFDs are found in some of the oldest craters on Mars, the deposits are clearly much younger than the craters themselves. Crater counts of the south polar layered terrain have resulted in a surface age estimation of about 10 Ma (Herkenhoff & Plaut, 2000). The

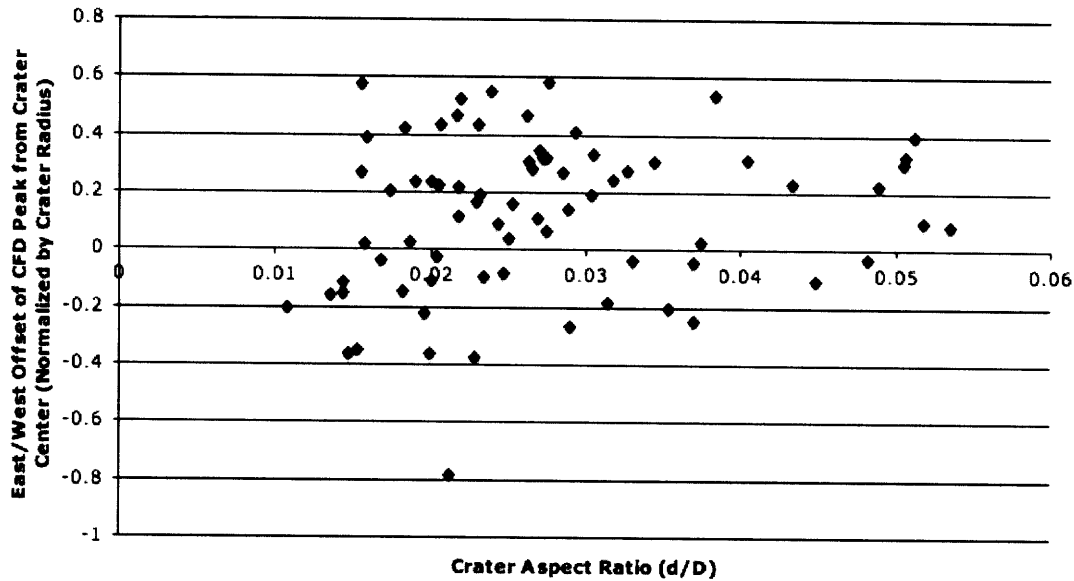


Figure 3-17: The east/west offset of the CFD peak from crater center, normalized by crater radius, plotted against the crater aspect ratio (d/D). A positive value indicates a westward offset; a negative value an eastward offset. The craters with the highest aspect ratios tend to exhibit westward CFD offsets.

apparently much younger NPLD have a more uncertain surface age because of a paucity of impact craters, but appear to be at most 100 ka (Herkenhoff & Plaut, 2000). The age of these CFDs, if they could be determined, would provide an important modeling constraint and could answer whether they were formed concurrently with the main PLD or on a different timescale. However, it cannot be assumed that all deposits formed simultaneously, so each deposit must be dated separately through crater counting, a task made very difficult by the low crater densities and surface area of each crater deposit. In no cases were we able to detect sufficient craters on the surfaces of the deposits to enable statistically significant crater counting.

3.3 Crater Insolation

Average annual insolation maps were created for all 75 craters containing CFDs. The computationally demanding full shadowing analyses were run on a subset of 7 of these, selected

to have a variety of deposit fill percentages and to cover the full geographic range of deposit occurrences.

To first order, variations in average annual insolation within these craters correlate poorly with deposit shape (Figures 3-6 – 3-10). Where such correlations do exist, they tend to show that the greatest insolation levels are found directly on the deposits (Figure 3-2), a misleading result given the presumed ice content of the deposits.

In addition, comparison of average annual flux maps both with and without shadowing included reveals that the effects of shadowing on the insolation received by a given point on the surface is minor compared to the influence of the slope and aspect of the terrain. Shadowing effects are greatest on the inside of a polar crater's poleward-facing walls, but most CFDs are detached from the crater wall.

Crater Name	Latitude (Deg N)	Longitude (Deg E)	Diam. (km)	Depth (km)	Aspect Ratio (d/D)	CFD Peak Offset (Scaled)	N/S Offset (Scaled)	E/W Offset (Scaled)	Layers Visible	Edge Ridges	Stacked Mounds	Flow Feat.	Sand Dunes	Geologic Unit
—	-80.95	69.87	27.8	1.44	0.052	0.337	-0.339	0.101	n	n	n	n	n	Apb
—	-79.93	-124.95	56.1	1.10	0.020	0.797	0.756	-0.224	y	n	y	y	n	Nhc
—	-79.29	-131.59	48.9	0.98	0.020	0.798	0.699	-0.362	y	y	n	y	n	Nhc
—	-78.94	-143.53	55.3	0.86	0.015	0.588	0.085	0.575	y	n	n	y	n	Nhc
Playfair	-78.32	-126.03	64.9	1.52	0.023	0.188	0.163	-0.095	y	n	y	n	n	Nhc
—	-77.57	-133.93	27.8	0.61	0.022	0.348	-0.297	0.119	n	n	n	n	n	Nhc
South	-77.41	21.79	107.3	1.69	0.016	0.221	0.220	0.021	y	y	y	y	n	HNk
—	-76.77	-134.85	37.9	0.88	0.023	0.20	0.0	0.192	n	n	n	n	n	Nhc
—	-76.13	-167.4	26.2	0.79	0.030	0.202	-0.045	0.194	n	n	n	n	n	HNpd
—	-76.1	-147.22	24.2	0.53	0.022	0.54	-0.097	0.526	y	n	n	n	n	HNpd
—	-75.81	-164.96	19.9	0.74	0.037	0.165	0.178	0.029	n	n	n	n	n	HNpd
—	-75.29	-173.3	65.5	1.04	0.016	0.714	0.576	0.393	y	n	y	y	n	Nhc
—	-75.13	-136.88	23.7	0.65	0.027	0.322	0.299	0.064	n	n	n	n	n	Nplc
—	-75.02	-165.66	54.1	1.29	0.024	0.785	0.544	0.553	y	y	y	y	n	Nhc
Reynolds	-75	-157.9	98	—	—	—	—	—	y	y	y	y	y	HNpd
—	-74.52	-143.03	27.2	0.74	0.027	0.356	-0.087	0.324	n	n	n	n	n	Nhc
—	-74.41	-125.4	47.3	1.09	0.023	0.464	-0.125	0.436	y	n	n	n	n	Nhc
—	-74.37	-130.59	58.6	1.69	0.029	0.437	-0.402	0.142	y	y	n	n	n	Nhc
—	-73.82	-106.06	25.3	0.79	0.031	0.431	-0.373	-0.182	n	n	n	n	n	Nhc
—	-73.76	-135.30	65.0	1.64	0.025	0.188	0.091	0.162	y	n	n	n	n	Nhc
—	-73.38	-155.56	54.9	1.89	0.034	0.535	0.408	0.311	y	n	n	n	n	Nhc
—	-73.18	-129.32	31.2	0.90	0.029	0.551	-0.453	-0.263	n	n	n	n	n	Nhc
—	-73.07	-80.86	34.0	1.72	0.051	0.313	0.035	0.302	n	n	n	n	n	Nhc
—	-73.07	-115.98	48.0	0.96	0.020	0.354	-0.270	0.235	n	n	n	n	n	Nhc
Burroughs	-72.82	116.84	109.4	2.23	0.020	0.160	0.162	-0.025	y	n	n	n	n	Nhc
—	-72.66	-117.94	25.3	1.35	0.054	0.095	-0.047	0.083	n	n	n	n	n	Nhc
—	-72.57	110.31	51.4	0.89	0.017	0.254	0.137	0.206	y	n	n	n	n	Nhc
Richardson	-72.4	179.6	96	—	—	—	—	—	y	y	y	y	y	Nhc
—	-72.25	-35.73	24.6	0.91	0.037	0.051	0.000	-0.044	n	n	n	n	n	Nhc
—	-72.06	-79.5	37.3	0.81	0.022	0.775	-0.600	0.469	n	n	n	n	n	Nhc
—	-71.79	-179.8	47.4	0.79	0.017	0.662	-0.646	-0.039	y	n	n	n	y	Nhc
—	-71.54	-130.93	80.9	1.86	0.023	0.422	-0.379	0.167	n	n	n	n	n	Nhc
—	-71.48	-143.73	55.0	1.36	0.025	0.099	-0.064	-0.082	y	n	n	n	y	Nhc
—	-71.15	158.71	46.0	1.63	0.035	0.669	-0.615	-0.200	n	n	n	n	y	Nhc
—	-70.95	106.36	19.9	0.66	0.033	0.576	-0.533	-0.039	y	n	n	n	n	Nhc
—	-70.74	-106.23	30.1	0.73	0.024	0.467	-0.469	0.091	n	n	n	n	n	Nhc
—	-70.61	-178.85	25.0	1.21	0.048	0.23	-0.235	-0.031	n	n	n	n	n	Nhc
—	-70.58	111.55	32.0	1.22	0.038	0.602	-0.258	0.540	y	n	n	n	n	Nhc
Agassiz	-70.55	-89.06	114.1	1.77	0.016	0.311	0.134	0.271	y	n	n	n	n	Nhc
—	-70.41	175.02	21.8	0.47	0.022	0.233	-0.054	0.217	n	n	n	n	n	Nhc

Table 3.1: Physical parameters and morphologies of 75 south polar crater-filling deposits and their host craters. Crater diameter is derived from the average rim-to-rim distance measured from eight transects. Crater depth is the average minimum elevation extracted from those transects. CFD peak offsets are scaled by the crater radius, so that an offset of 0.5 places the CFD peak halfway between the crater’s center and rim. Northward and westward CFD peak offsets are positive; southward and eastward offsets are negative. Continued on the following page.

Crater Name	Latitude (Deg N)	Longitude (Deg E)	Diam. (km)	Depth (km)	Aspect Ratio	CFD Peak Offset	N/S Offset	E/W Offset	Layers Visible	Edge Ridges	Stacked Mounds	Flow Feat.	Sand Dunes	Geologic Unit
Jeans	-70.32	154.05	79.4	1.16	0.015	0.376	-0.030	-0.360	y	n	n	n	y	Nhc
—	-70.18	180.29	47.8	0.99	0.021	0.396	-0.345	0.436	n	n	n	n	n	Nhc
—	-69.95	-153.8	40.7	1.12	0.028	0.61	0.116	0.585	n	n	n	n	n	Nhc
—	-69.95	-129.24	47.2	1.18	0.025	0.207	-0.200	0.043	y	n	n	n	y	Nhc
—	-69.81	116.08	46.7	0.94	0.020	0.412	-0.404	-0.105	y	n	n	n	n	Nhc
—	-69.66	155.83	46.6	1.26	0.027	0.486	-0.329	0.344	n	n	n	n	n	Nhc
—	-69.54	-150.13	64.1	1.68	0.026	0.5	0.110	0.468	n	n	n	n	n	Nhc
—	-69.36	162.49	42.5	0.79	0.019	0.839	-0.805	0.030	y	y	n	n	y	Nhc
Charlier	-69.23	-168.69	110.6	1.59	0.014	0.600	-0.565	-0.149	y	y	n	n	y	Nhc
—	-68.91	151.16	42.1	1.12	0.027	0.335	-0.168	0.282	y	n	n	n	n	Nhc
—	-68.68	162.91	28.2	0.58	0.021	0.344	-0.209	0.228	n	y	n	n	y	Nhc
—	-68.59	170.32	43.5	1.32	0.030	0.447	0.271	0.336	n	n	n	n	n	Nhc
—	-68.4	152.98	45.4	0.49	0.011	0.4499	-0.393	-0.202	n	n	n	n	n	Nhc
—	-67.94	171.02	40.2	1.31	0.033	0.299	0.088	0.275	n	n	n	n	n	Nhc
Suess	-67.64	-178.75	70.6	1.94	0.027	0.457	0.301	0.323	y	y	n	n	n	Nhc
—	-67.6	117.69	36.2	0.97	0.027	0.437	-0.391	0.112	y	n	n	n	n	Nhc
—	-67.46	162.54	20.4	0.37	0.018	0.444	0.058	0.421	n	n	n	n	n	Nhc
—	-67.43	160.82	27.2	0.58	0.021	0.835	-0.173	-0.781	n	n	n	n	y	Nhc
—	-67.41	-164.4	50.4	1.86	0.037	0.523	-0.421	-0.244	n	n	n	n	y	Nhc
—	-66.94	151.14	47.8	0.65	0.014	0.459	-0.419	-0.155	y	n	n	n	n	Nhc
—	-66.9	165.06	34.2	0.97	0.028	0.373	0.206	0.270	n	n	n	n	n	Nhc
—	-66.89	148.85	22.2	0.99	0.045	0.199	-0.159	-0.104	n	n	n	n	n	Nhc
—	-66.82	120.83	32.2	1.02	0.032	0.268	-0.110	0.245	y	n	n	n	n	Nhc
—	-66.81	161.25	33.6	0.77	0.023	0.383	0.035	-0.373	n	n	n	n	y	Nhc
—	-66.8	169.87	49.4	0.94	0.019	0.482	-0.406	0.236	n	n	n	n	y	Nhc
—	-66.25	-124.45	18.6	0.94	0.051	0.678	0.569	0.330	n	n	n	n	n	Nhc
—	-66.08	120.12	49.8	1.31	0.026	0.327	0.071	0.307	y	n	n	n	n	Nhc
—	-66.02	144.19	56.9	0.87	0.015	0.508	-0.352	-0.347	n	n	n	n	y	Nplc
—	-65.6	171.23	53.4	0.77	0.014	0.356	-0.309	-0.110	n	n	n	n	y	Nhc
—	-65.34	158.39	38.4	1.66	0.043	0.352	-0.246	0.231	y	n	n	n	y	Nhc
—	-64.91	176.69	49.6	2.00	0.040	0.329	0.024	0.313	n	n	n	n	n	Nhc
—	-64.85	155.91	27.1	0.49	0.018	0.195	0.130	-0.148	n	n	n	n	n	Nhc
—	-64.6	-142.88	37.9	1.11	0.029	0.431	0.031	0.413	n	n	n	n	n	Nplc
—	-62.1	132.62	28.0	1.43	0.051	0.68	-0.505	0.395	y	n	n	n	n	Nhc
—	-60.8	133.65	35.4	1.73	0.049	0.252	-0.033	0.228	y	n	n	n	n	Nhc
Mean	-70.88	-2.03	45.1	1.13	0.027	0.42	-0.087	0.12	n/a	n/a	n/a	n/a	n/a	n/a
Std. Error	—	—	2.5	0.051	0.001	0.02	0.039	0.032	n/a	n/a	n/a	n/a	n/a	n/a
Median	-70.55	-80.18	42.5	1.02	0.025	0.41	-0.064	0.17	n/a	n/a	n/a	n/a	n/a	n/a
Med. Error	—	—	3.1	0.064	0.002	0.03	0.048	0.040	n/a	n/a	n/a	n/a	n/a	n/a
Std. Dev.	4.30	143.46	21.4	0.43	0.011	0.19	0.329	0.27	n/a	n/a	n/a	n/a	n/a	n/a

Table 3.2: *Continued from Table 3.1.* Physical parameters and morphologies of 75 south polar crater-filling deposits and their host craters. Crater diameter is derived from the average rim-to-rim distance measured from eight transects. Crater depth is the average minimum elevation extracted from those transects. CFD Peak offset is scaled by the crater radius, so that an offset of 0.5 places the CFD peak halfway between the crater's center and rim. Northward and westward CFD peak offsets are positive; southward and eastward offsets are negative.

Chapter 4

Discussion

4.1 Deposit Composition

While the dusty surfaces of the CFDs preclude straightforward estimates of composition, it does seem clear that these deposits contain significant amounts of water ice. Their proximity and morphological similarity to the main SPLD, including internal layering, imply a parallel formation history and thus composition. The composition of the SPLD itself and the stability of water ice in the polar regions have been the subject of much study (see Kolb & Tanaka (2001) for a detailed discussion of the composition and history of the SPLD). Although the SPLD has long been thought to consist of a mixture of dust and water ice (Cutts, 1973), the exact proportions of each remain unknown. The best constraint to date comes from Zuber et al. (2007), who calculated a density consistent with water ice and $\sim 15\%$ admixed dust. However, the decreasing stability of water ice farther from the poles and the existence of morphologically similar crater deposits in equatorial regions (Russell & Head, 2005) suggest that the ice content in these CFDs may drop with distance from the poles. Kolb & Tanaka (2001) note that the physical properties of icy deposits are very sensitive to the relative proportions of ice and impurities, and we may thus expect very different responses to the same forcings if these CFDs vary in composition. Any response to solar forcing, however, is a strong indication of volatile content within the deposits.

Some direct measurements of CFD composition have been made. Kuti (2009) monitored the albedo and thermal conditions for an analogous mounded deposit in the north polar region residing in Dokka Crater, finding that the high summertime albedo of the deposit was strongly suggestive of water ice. Morphological similarities between deposits in the northern and southern hemispheres suggest that both sets of deposits have roughly the same composition. Observations made on the Richardson Crater CFD with the Compact Reconnaissance Imaging Spectrometer for Mars (CRISM) show water ice and sand visible through dark patches of defrosting carbon dioxide ice on the surface.¹

4.2 Deposit Morphology

By our definition, these crater-filling deposits fit a simple set of morphological criteria: a raised, flat-topped mound, clearly of secondary fill material, with a distinct boundary between crater floor and deposit. All features that match this definition may not necessarily share the same composition, formation mechanism, or modification history. Interpretation of crater deposits therefore offers an additional set of complications above and beyond their simple identification. Distinguishing between a mound of outlying layered deposit material mantled by dust and sand as opposed to mounded sand dunes covered with icy frost is difficult at best with the available datasets. In addition, observations of dune fields overlying portions of the main SPLD (Malin & Edgett, 2001) raise the possibility that deposits appearing to be sand dunes may in fact hide ice underneath. Much interpretation must therefore be done on the basis of observed characteristics and modeling of the physical conditions within the craters.

Russell & Head (2005) identified four classes of crater fill: "Embedded," "Lobe," "Center," and "Remnant." While most observed deposits can be sorted into one or more of these descriptive categories, this nomenclature is predicated on the hypothesis that the crater deposits observed today formed as part of a once-larger contiguous ice sheet. Such a scenario would imply that the degree of erosion and degradation each CFD has experienced is di-

¹http://crism.jhuapl.edu/gallery/featuredImage/image.php?image_id=87

rectly related to its distance from the main SPLD and percentage of crater fill. However, the past extent of the SPLD is by no means clear, and some deposits which Russell & Head (2005) might classify as "Remnant" may in fact be near their maximum size if they formed in isolation within their host crater rather than being left behind by a retreating ice sheet. In this case, the composition and degree of erosion of deposits of similar fill percentages may vary substantially.

One significant question regarding the morphology of these CFDs is the role viscous flow has played in their evolution. Disagreement persists over the degree to which the polar layered deposits themselves exhibit signatures of plastic deformation and viscous flow. There is a general lack of observed flow features in the layered deposits (Herkenhoff & Plaut, 2000), though multiple examples exist near the south pole of extensions of the layered deposits into adjacent impact craters. Several authors have examined one of these craters, located near the mouth of the Chasma Australe, into which a tongue of the the SPLD extends. Whether this feature displays evidence of the flow and lateral movement of the layered deposits themselves (Head, 2000; Hartmann, 2000) or simply the partial retreat of undeformed layered deposits (Kolb & Tanaka, 2001) has not been resolved. The fact that such lobes have not completely overtaken the low-lying craters into which they extend suggests that minimal lateral movement has taken place (Kolb & Tanaka, 2001).

Studies of the north polar layered deposits suggest that the Martian ice caps are fairly stagnant in terms of flow. No convincing morphological evidence exists for glacial flow induced by basal melting in the PLD, and windows of unscoured underlying terrain within the SPLD argue against significant glacial movement (Kolb & Tanaka, 2001). The internal temperatures and pressures calculated for the ice caps appear to be far too low for basal melting to occur (Greve et al., 2004), though slow viscous creep of water ice will occur at the entire range of planetary conditions (Durham et al., 1992). Using analytical techniques, Fisher (1993) examined the north polar ice cap of Mars and calculated an outward flow rate of 3 mm/yr. Greve et al. (2004) employed finite element modeling of a north polar cap composed of pure ice and found flow velocities on order of 1 mm/yr. At Martian surface

conditions, a dust content of $\sim 10\%$, similar to that posited for the SPLD (Zuber et al., 2007), actually leads to an ice hardness nearly twice that of pure water ice (Greve et al., 2005; Durham et al., 1992). These results strongly indicate that the present topography of the north polar cap, and by analogy the south polar cap as well, is overwhelmingly controlled by the surface mass balance rather than ice flow (Greve et al., 2004; Kolb & Tanaka, 2001).

The similarities of these CFDs to the SPLD, along with their typical mounded shape and steep bounding slope, indicate that viscous flow is less important than other processes in shaping the deposits. The morphology of the CFDs in craters such as Reynolds and Richardson is thus difficult to interpret. These CFDs feature lobes on the order of 50 km long extending between adjacent craters. These lobes seem to exhibit a clear directionality of flow away from the pole, but at flow rates of 1 mm/yr or less, these features would have taken more than 50 Ma to extend to their current dimensions, a time scale greater than the estimated age of the SPLD (Herkenhoff & Plaut, 2000). Unless these CFDs experienced dramatically faster flow rates than is predicted for SPLD material, their morphologies must be primarily the expression of other mass-balance processes, including both ice deposition and growth over the existing topography and erosion and retreat through solar and eolian ablation responsible for their current morphology. SHARAD radargrams of the unnamed crater adjacent to the SPLD at 79.9° S, -125.0° E, seem to support this interpretation. Despite sloping deposit material that could be plausibly be thought to have flowed in from the SPLD, depth-corrected radargrams of the deposit reveal layers that are roughly parallel to the deposit surface and to each other, apparently undisturbed by flow. Other features in these deposits, such as the edge ridges evident in the CFDs in Reynolds Crater and South Crater (Byrne, 2003), could result from compression during flow, though in the next section we will explore alternative explanations as well.

4.3 The Polar Crater Micro-environment

Because these mounded deposits are found inside craters that are situated in otherwise ice-free terrain near the PLD, the crater micro-environment appears to be crucial to CFD

formation and modification. As large topographic depressions, Martian polar craters experience different insolation conditions, wind patterns, atmospheric conditions, and eolian sediment loads than the surrounding terrain. Each of these factors may influence deposit formation and evolution, though determining the relative contributions of each process is a complicated task.

4.3.1 Solar Insolation

The strong north or south offsets of some CFDs within their host crater makes it plausible to surmise that solar heating and shadowing by the crater rim play a role in controlling the stability zones of the deposits. However, our results imply a minimal direct role for shadowing in deposit preservation. The vast majority of the measured crater deposits lie in craters with a diameter of at least 20 km. At this size, Martian craters are flat-floored, generally with a relatively shallow profile (Melosh, 1989). In fact, the aspect ratio of craters containing CFDs is usually low enough that, even when shadowing effects are considered, only the inside of the crater walls and the crater floor adjacent to the walls experience an appreciably decreased solar flux compared to the terrain immediately outside the crater. If shadowing were the predominant influence on the morphology of these deposits, we would expect most deposits to be nestled up against the northern (poleward-facing) wall of the crater, while almost all observed deposits currently lie beyond the rim's protective shadow.

In fact, the majority of CFDs are actually offset south of the center of their host crater. This result is consistent with solar ablation of the northern, equator-facing slopes of icy deposits rather than shadowing. Any deposit situated beyond the protective shadow of the crater's poleward-facing wall will receive the highest solar flux on its northern, equator-facing slopes. This effect appears to be much more significant than shadowing, especially in the deepest craters, whose deposits are most consistently offset southward. This result is further supported by energy balance modeling of a hypothetical polar crater filled with ice in the northern hemisphere by Russell et al. (2004). Their modeling revealed that troughs in the ice begin to form within a year between the deposit and the crater wall, with a deeper and

wider trough forming on the equator-facing side of the deposit.

The correlation between the higher amount of solar energy received by the northward-facing slopes of the deposits and the tendency of deposits to be offset southward are strong confirmations of the presence of volatiles within these deposits. A consistent poleward offset would be difficult to explain for deposits composed entirely of non-volatile fill, such as sand or dust. Regardless of the original proportion of sand or dust in the deposits, however, the ablation of near-surface volatiles is likely to concentrate those non-volatiles in an surface lag that could protect the CFD against further ablation. As little as a few millimeters of fine dust at the current latitudes of the SPLD may be sufficient to prevent ice sublimation during the summer (Keller, 2000). The low apparent thermal inertia of the SPLD surface strongly indicates that such a lag is in fact present (Paige & Keegan, 1994). The morphologies seen today in CFDs may therefore represent a balance between solar-driven sublimation and thickening of a dust lag, though the long-term stability of these deposits under current climatic conditions is unclear.

The effects of solar insolation may also be expressed in the edge ridges seen in the deposits in Reynolds Crater, South Crater, and others. Terrestrial observations of dry valley glaciers in Antarctica led Hughes (1975) to propose that differential solar ablation of bands of ice with varying albedos could lead to the formation of surface waves in the ice. On Mars, icy CFDs with exposed layering could form the observed ridges in much the same way, with layers of differing dust content absorbing varying amounts of solar radiation. Once ridges were initially established in the topography, whether through differential absorption of sunlight, compression during flow, or the placement of parallel dunes, then solar ablation could serve to enlarge and deepen the ridges, as the equatorward-facing slopes would receive more insolation than poleward-facing terrain. Our predictions of average annual insolation confirm that a $\sim 10\%$ difference in insolation between poleward and equatorward-facing slopes can occur in this way (Figures 3-6, 3-9).

4.3.2 Crater Winds, Eolian Sediment Transport, and Atmospheric Conditions

The polar regions, and the layered deposits in particular, display the work of extensive eolian modification. Dune fields, wind streaks, scarps, and spiral troughs are all the result of wind erosion and transport over long time periods (Howard, 2000). While the general extent of the SPLD is roughly controlled by latitude, the specific boundary and morphology of the SPLD appear to be largely controlled by eolian processes. Similarly, while the latitudinal distribution of CFDs may be largely dependent on the available solar flux, the specific shapes of each deposit are likely heavily affected by eolian erosion and deposition. CFDs do exhibit signs of eolian influence on their surfaces. In particular, the tendency for the highest point of the CFD to be offset to the west of the crater center is consistent with Coriolis deflection of regional katabatic winds in the southern hemisphere. Surface evidence and modeling indicate that these exceptionally powerful and consistent winds blow outward from the polar cap (Toigo et al., 2002), with sustained winds of 10 m/s and gusts of up to 50 m/s (Howard, 2000). Those CFDs in craters with particularly high measured aspect ratios (greater than 0.04) overwhelmingly exhibit a westward offset, possibly indicating that the effects of these winds are strengthened in deeper craters.

Our knowledge of Martian surface winds is poorly constrained. Aside from wind data at the Viking Lander and Mars Pathfinder sites, no direct measurements of Martian surface winds are available. Local wind conditions must therefore be either modeled or inferred from their expression in surface features. One of the best indirect means of studying surface winds is through sand dune morphology and orientation. Martian craters have previously been noted for their ability to act as traps for windblown sand (Breed et al., 1979; Anderson et al., 1999). Extensive sand dune fields are found in a variety of terrains on Mars, including the floors of craters throughout the southern hemisphere. These dunes most commonly take the form of crescentic ridges (Breed et al., 1979). Dune slip faces on these ridges form by oversteepening of the dune brought on by saltating sand carried by the wind to the edge of the slip face. These slip faces therefore reflect the local wind regime, facing the opposite

direction from which the wind blows. Careful measurement of dune orientations can be used to reconstruct prevailing wind patterns (Fenton & Bandfield, 2003). Dunes can be found on the surface of numerous CFDs, most notably in Richardson Crater, and their presence may offer a means of constraining wind patterns in their host craters. Hovius et al. (2009) have conducted just such a study for CFDs in Mars' north polar region. They found that, close to the pole, the asymmetries in the ice deposit shapes seem to be correlated with the dominant prevailing wind recorded in dune slip faces, while away from the pole, the deposit shapes are oriented away or perpendicular to the wind.

In addition, recent improvements in mesoscale modeling have made it possible to model local wind patterns at a spatial scale comparable to that of an impact crater. Kuzmin et al. (2001) modeled airflow over a simulated 1 km-diameter crater and showed that the maximum wind stresses occur on the downwind crater rim. For these deposit-containing polar craters, the prevailing winds are likely southerly, away from the pole, suggesting that the poleward offsets observed in many CFDs may be partly the result of erosion of the northern side of the deposits by polar katabatic winds. These katabatic winds are strongest during the Martian spring and summer, when the temperature gradient from the pole to the surrounding terrain is greatest (Howard, 2000), and during this period, they are able to entrain sand and dust for transport (Toigo et al., 2002). Mesoscale modeling has shown that these katabatic winds can accelerate into topographic lows, and that they are most effective at carrying sand at latitudes poleward of 50° (Fenton et al., 2004).

While these katabatic flows may dominate regional wind conditions, the dunefields of craters throughout the southern highlands show evidence of a multi-directional wind regime that varies throughout the Martian year and from location to location (Fenton et al., 2004). Fenton et al. (2005) modeled wind patterns in and around Proctor Crater, a 150 km diameter crater in the southern highlands containing a large dune field and other features suggestive of wind direction. Comparing their modeling results with wind directions predicted from dune slip faces (Fenton & Bandfield, 2003), they found that two of the three prevailing wind directions expressed in the dune forms were predicted by their model. Their modeling

showed that crater winds can be highly variable on both seasonal and diurnal time scales, and that the topographic presence of a crater will significantly modify the local wind regime, both in direction and magnitude. For instance, incoming air may accelerate as it falls from crater rim to floor. This irregularity of crater wind patterns may be responsible for the asymmetries seen in most CFDs.

While crater wind patterns are gradually becoming clearer, the effects of the crater topography on other atmospheric parameters such as air temperature remain incompletely understood. Whiteman et al. (2008) have observed that Arizona’s Barringer Meteor Crater experiences temperature inversions, especially during the winter, in which the crater floor is up to 15 °C colder than the crater rim. These inversions, the result of the topographic depression provided by the 1-km crater, form in the late afternoon to evening in the absence of strong background flows. If Martian craters 20–110 km in diameter are similarly able to act as cold traps, then they could provide sheltering conditions for icy deposits unable to persist directly outside the craters. Hovius et al. (2009) claim that the deposits in the north polar region do not coincide with present-day cold traps as determined from frost patterns, but such an evaluation has not been undertaken for the south polar region.

4.3.3 Crater Dune Fields and Seasonal Frost

Malin & Edgett (2001) note that sand appears to be a controlling factor in the formation of seasonal frost in the fall and winter and the disappearance of that frost in the spring. In particular, frost forms first on sand dunes in the fall and winter, and, though dune frost is the first to start to disappear in the spring, frost persists on some south polar dunes until mid-summer (Malin & Edgett, 2001). Year-long observations of icy dunes in Richardson Crater (72.4° S, 179.6° E) made with the MGS Thermal Emission Spectrometer (TES) (Christensen et al., 2001) show that dune temperatures range from around the freezing point of CO₂ (~148 K) in the late winter to just under the freezing point of H₂O (273 K) in mid-summer, when the dunes appear frost-free (Edgett et al., 2000; Supulver et al., 2001). The same dunes were later imaged at the beginning of the southern spring with CRISM, which identified

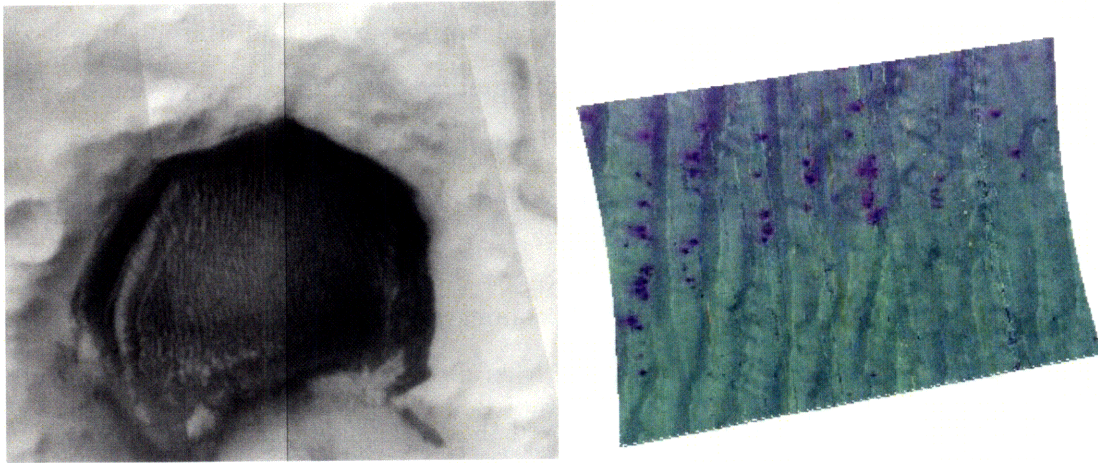


Figure 4-1: *Left* : MOC mosaic of dark sand dunes atop a CFD in Richardson Crater, at 72.4° S, 179.6° E (courtesy www.google.com/mars). *Right* : CRISM spectral map of Richardson Crater dunes overlaid on a surface brightness map. Sand is red, H_2O ice is blue, and CO_2 ice green. Both H_2O and CO_2 ices are present in the blue-green areas; purple areas contain both H_2O ice and sand (http://crism.jhuapl.edu/gallery/featuredImage/image.php?image_id=87).

the frost as a mixture of CO_2 and water ice (Figure 4-1).² Fenton et al. (2005) note that dunes in Proctor Crater, much closer to the equator, also experience frost during the winter months that may impede eolian movement of the dunes. In light of these observations, Malin & Edgett (2001) suggest that porous sand dunes may "breathe" water vapor or that some combination of the thermophysical properties of sand and the microstructure of the dune surfaces may enhance the deposition and preservation of frost.

These seasonal frost observations may provide important clues to the origins of CFDs. If sand dunes can act as a substrate for the crystallization of water ice, then they could provide a means for ice deposits to form within craters but not directly outside them. In the current climate epoch, water ice frost does not persist year-round outside of the PLD, but if, under past climatic conditions, crater dunes were able to inhibit the seasonal sublimation of frost to the extent that some frost persisted year-round, then mounded, layered deposits could be slowly built up over time. As measured by TES, the albedo of water ice frost (~ 0.35) is much higher than that of sand (~ 0.15) (Supulver et al., 2001). The presence of this frost on dune

²http://crism.jhuapl.edu/gallery/featuredImage/image.php?image_id=87

surfaces would therefore further reduce the amount of solar energy absorbed by the dunes and promote additional frost deposition. Gradual mantling by continuing dust and sand deposition would help preserve existing ice from ablation. In turn, the condensation of ices within and on top of the dunes would serve to immobilize sand grains and dust (Ahlbrandt et al., 1978).

The strength of the various feedback processes outlined above and their capability to enhance the amount of water ice retained by sand dunes are poorly known or constrained. This dune frost scenario can qualitatively explain many of the observed characteristics of CFDs, however, without necessitating the past expansion of the SPLD by hundreds of km towards the equator. While this mechanism does suggest that the stability zone of water ice was once extended equatorward from its current range, as proposed by Head et al. (2003), it does not require that the past extent of the SPLD was significantly different from its current expanse. Russell & Head (2005) propose that the crater deposits persist after the sublimation of similar deposits outside the craters because their formation in a depression allows for a greater initial thickness, but they do not detail any mechanism by which this initial thickening could occur. The crater microenvironment, including any enhancements by sand dunes in ice deposit formation, can explain not only why CFDs appear only within craters, but also why only certain craters contain deposits. Not all craters will be able to accumulate and retain sufficient sand to form the dune fields needed to act as deposit substrates. Smaller craters will capture less sand because of their smaller areas and depths. Shallow craters will be less able to capture sand because of their smaller potential energy well. In addition, Fenton et al. (2005) note that sand loss and dune migration in Proctor Crater may be inhibited by the opposing prevailing winds. Whether stable dunes or ice deposits can persist in a particular crater may thus depend on the local wind regime, just as the ability of a crater to act as a cold trap may depend on its specific geometry and location. More modeling and observations of local wind conditions in the polar regions will be necessary to further constrain the role of sand dunes in CFD formation and modification.

4.4 Deposit Origin and Evolution

The CFDs we have mapped and studied appear to be the expression of gradual processes operating over long periods of time. The internal layering detectable in many CFDs points to an origin through seasonal or interannual deposition, inconsistent with episodic formation processes such as glacial ice flow or groundwater release. The trends of decreasing crater fill size and increasing deposit asymmetry at lower latitudes are strong indications of a climatic control on CFD formation and modification. Variations in orbital parameters such as obliquity have previously been identified as likely forcing factors in the polar layered deposits (Laskar et al., 2002). Head et al. (2003) has proposed that periods of high obliquity would cause the stability zone for water ice to move toward the equator, leading to glaciation at Martian mid-latitudes. If these deposits are the remnants from a period when the extent of the SPLD once was much greater (Russell et al., 2004; Russell & Head, 2005), it would imply that significantly different climatic conditions were present within roughly the last 10 Ma, the estimated surface age of the SPLD (Herkenhoff & Plaut, 2000). Certainly, the lack of craters on existing CFDs suggests that their ages do not greatly exceed this 10 Ma timeframe.

Distinguishing whether these crater ice deposits formed in isolation or as part of a once-larger polar ice sheet is a challenging proposition, particularly as all deposits may not share identical origins and evolutionary histories. The layering within these CFDs remains the key to their interpretation. If the deposits formed in isolation from the SPLD within these craters, we would expect concave-down or flat layering within the deposits, as is seen in SHARAD radargrams of the Burroughs Crater CFD (Figure 3-3). If instead, the deposits formed within a larger ice sheet, we would expect the layered ice deposits to be draped fairly evenly over the landscape, with the layering within craters curving upward at the crater walls. While we do not observe any deposits with clearly upturned layering, differentiating among layering patterns is made difficult by the fact that most CFDs are detached from the crater wall, where the underlying topography steepens the most.

While most CFDs likely formed in isolation, those closest to the SPLD, often consisting

of multiple stacked mounds, may have once been part of a larger ice sheet. Radargrams of an unnamed crater directly outside the SPLD at 79.9° S, -125.0° E exhibit layering in a CFD consisting of two stacked mounds. These layers are parallel to the deposit surface rather than the crater floor, suggesting that they have been laid atop the pre-existing lower mound rather than accumulating continuously upward from the crater floor. This structure is consistent with an initial episode of deposition within the crater followed by deposition on a more regional scale. In this scenario, the SPLD may once have completely or partially engulfed this crater, eventually retreating and leaving a remnant atop the lower original mound.

Even if the SPLD once extended to lower latitudes, it does not necessarily follow that all CFDs are remnants of the SPLD. Given that these deposits persist today within craters situated in otherwise ice-free terrain, they may also have been able to accumulate within these craters at times when permanent ice deposition could not occur in the surrounding area. In addition, if the south polar regions were in fact once covered with layered deposits down to a latitude of $\sim 60^{\circ}$ S, we would expect to see evidence of glacial activity in the recent past. While Head & Pratt (2001) cite morphological indications of the presence of a massive ice sheet reaching the southern mid-latitudes in the Hesperian period (3.5 to 1.8 Ga), signs of a more recent epoch of extensive glaciation remain elusive.

Regardless of the past extent of the SPLD, it seems highly likely that these CFDs were formed during a different climatic regime than the present. Exposed layering on many CFDs indicates that we are currently in an ablative regime rather than an accumulative one. Layering is generally less visible in deposits farther from the SPLD, whether subject to a higher degree of erosion, obscured by windblown sediments or a dust lag or never present in the first place. The presence of deposits with multiple superposed mounds may imply that repeated ice deposition and erosion episodes occurred over the history of these deposits, the result of corresponding swings in the climate of the south polar region. Alternatively, the darker lower mounds could represent dust or sand-rich layers more resistant to erosion than the more ice-rich upper layers. Whatever the details of their interpretation, these CFDs

show signs of the influence of multiple distinct climate regimes in the south polar region over the last ~ 10 Ma, with the stability zone of water ice periodically expanding and contracting.

Chapter 5

Conclusions

The crater-filling deposits near the south pole are the expression of a complex interplay of multiple processes. Most likely originating under different climatic conditions than those of the present day, these CFDs now experience an erosive climate regime and exhibit signs of being shaped by wind and sun. The deposits and their host craters display morphologies and physical properties that are consistent with solar ablation and eolian erosion, while shadowing by the crater topography appears to be of minimal importance in preserving the deposits. The morphology and layering of many of these deposits suggests that they are outliers of the polar layered deposits, but it remains uncertain whether they formed in isolation from the SPLD or were left behind by the retreat of a formerly larger ice sheet.

Our research suggests that the past extent of the polar layered deposits did not have to be substantially greater than it is at present to allow for the formation of these icy crater-filling deposits. Higher obliquities likely experienced over the past ~ 10 Ma would have caused the stability zone for water ice to move equatorward, as proposed by Head et al. (2003). The presence of sand dunes in these circumpolar craters may have provided a substrate for the preferential accumulation of water ice inside the craters, an effect possibly enhanced by atmospheric conditions created by the crater topography. Hundreds of thousands, if not millions, of years of accumulation gradually built up these CFDs to thicknesses of half a km or more. Then, as the planet's obliquity shifted towards its present value and the stability

zone of water ice retreated poleward, the deposits suffered erosion from solar heating and eolian forces. Deposits at lower latitudes would have had less time to accumulate and would have experienced erosion for longer, a trend reflected in increasing crater fill towards the pole. Deposits with stacked lobes suggest that such a cycle may have occurred multiple times in the history recorded in the deposits.

These crater deposits leave many further questions to be answered. Are the deposits composed primarily of water ice, sand, or dust, and in what proportions are these constituents present? How, if at all, does the presence of sand dunes inside polar craters encourage water ice or carbon dioxide frost accumulation? What role, if any, has viscous flow played in the formation and modification of the deposits? Do all deposits share similar formation histories, compositions, and internal structures? How does the history of these southern polar deposits compare with analogous deposits in the north polar region? To address these and other questions, additional observations and modeling will be needed. Spectroscopic observations with instruments such as CRISM are needed to constrain deposit surface composition, while further analysis of SHARAD radargrams may reveal additional clues as to the internal composition and structure of the deposits. Extended monitoring of seasonal processes such as the frost cycle might reveal some of the mass-balance mechanisms at work in these craters and in the SPLD proper. High-resolution modeling of crater winds, detailed energy balance modeling, and study of dune frost cycles within these polar craters will be similarly useful. Continued examination of these icy crater deposits is likely to prove fruitful, as their origin and modification is tied more broadly to polar volatile cycling mechanisms, the evolution of the SPLD, and recent Martian climatic history as a whole.

Bibliography

- Ahlbrandt, T. S., Fryberger, S. G., & Andrews, S., 1978, NASA TM-78,455, 1
- Anderson, F. S., Greeley, R., Xu, P., Lo, E., Blumberg, D. G., Haberle, R. M., & Murphy, J. R., 1999, Assessing the Martian surface distribution of aeolian sand using a Mars general circulation model, *J. Geophys. Res.*, 104, 18991
- Breed, C. S., Grolier, M. J., & McCauley, J. F., 1979, Morphology and Distribution of Common "Sand" Dunes on Mars: Comparison With the Earth, *J. Geophys. Res.*, 84, 8183
- Byrne, S., 2003, Implications of Flow and Brittle Fractures of Ice Masses in South Polar Craters. Sixth Int'l Conf. on Mars, 1 [Abstract]
- Christensen, P. R., Bandfield, J. L., Hamilton, V. E., Ruff, S. W., Kieffer, H. H., et al., 2001, Mars Global Surveyor Thermal Emission Spectrometer experiment: Investigation description and surface science results, *J. Geophys. Res.*, 106, 23823-23871
- Christensen, P. R., Jakosky, B. M., Kieffer, H. H., Malin, M. C., McSween, H. Y., Jr., Nealon, K., Mehall, G. L., Silverman, S. H., Ferry, S., Caplinger, M., & Ravine, M., 2004, *Space Sci. Rev.*, 110, 85-130
- Cutts, J. A., 1973, Nature and origin of layered deposits of Martian polar regions. *J. Geophys. Res.*, 78, 4231
- Douté, S. et al., 2007. South Pole of Mars: Nature and composition of the icy terrains from Mars Express OMEGA observations. *Planet. Space Sci.* 55, 113-133.

- Durham, W. B., Kirby, S. H., & Stern, L. A., 1992, Effects of dispersed particulates on the rheology of water ice at planetary conditions, *J. Geophys. Res.*, 97, 20883- 20897
- Edgett, K. S., Supulver, K. D., & Malin, M. C., 2000, Spring Defrosting of Martian Polar Regions: Mars Global Surveyor MOC and TES Monitoring of the Richardson Crater Dune Field, Second Int'l Conf. Mars Polar Science Exploration, LPI Contribution 1057, 34 [Abstract]
- Fenton, L. K. & Bandfield, J. L., 2003, Aeolian processes in Proctor Crater on Mars: Sedimentary history as analyzed from multiple data sets, *J. Geophys. Res.*, 108, 3-1
- Fenton, L. K., Toigo, A. D., & Richardson, M. I., 2004, Does the present-day wind regime explain the location and geomorphology of dunes in the southern highlands of Mars? American Geophys. Union, #P22A-05 [abstract]
- Fenton, L. K., Toigo, A. D., & Richardson, M. I., 2005, Aeolian processes in Proctor Crater on Mars: Mesoscale modeling of dune-forming winds, *J. Geophys. Res.*, 110
- Fisher, D. A., 1993, If Martian ice caps flow - Ablation mechanisms and appearance, *Icarus*, 105, 501-511
- Garvin, J. B., Sakimoto, S. E. H., & Frawley, J. J., 2003, Craters on Mars: Global Geometric Properties from Gridded MOLA Topography. Sixth Int'l Conf. on Mars
- Greve, R., Mahajan, R. A., Segschneider, & J., Grieger, B., 2004, Evolution of the north-polar cap of Mars: a modelling study, *Planetary and Space Sci.*, 52, 775-787
- Greve, R. & Mahajan, R. A., 2005, Influence of ice rheology and dust content on the dynamics of the north-polar cap of Mars, *Icarus*, 174, 475-485
- Hartmann, W. K., 2000, Polar Terrain and Youthful Geological Processes on Mars, Second Int'l Conf. Mars Polar Science Exploration, LPI Contribution 1057, 64 [Abstract]

- Head, J. W., 2000, Evidence for Geologically Recent Lateral Migration of Volatile-Rich Polar Layered Deposits, Second, Int'l Conf. Mars Polar Science Exploration, LPI Contribution 1057, 66 [Abstract]
- Head, J. W. & Pratt, S., 2001, Extensive Hesperian-aged south polar ice sheet on Mars: Evidence for massive melting and retreat, and lateral flow and ponding of meltwater, *J. Geophys. Res.*, 106, 12275-12299
- Head, J. W., Mustard, J. F., Kreslavsky, M. A., Milliken, R. E., & Marchant, D. R., 2003, Recent ice ages on Mars. *Nature*, 426, 797
- Herkenhoff, K. E., & Plaut, J. J., 2000, Surface Ages and Resurfacing Rates of the Polar Layered Deposits on Mars. *Icarus*, 144, 243
- Holt, J. W., Safaeinili, A., Plaut, J. J., Head, J. W., Phillips, R. J., Seu, R., Kempf, S. D., Choudhary, P., Young, D. A., Putzig, N. E., Biccari, D., & Gim, Y., 2008, Radar Sounding Evidence for Buried Glaciers in the Southern Mid-Latitudes of Mars: Supplementary Online Material, *Science*, 322, 1235-1238
- Hovius, N., Conway, S. J., Barnie, T. B., & Besserer, J., 2009, Ice Filled Craters in Mars' North Polar Region – Implications for Sub-Surface Volatiles, LPSC XL [Abstract]
- Howard, A. D., 2000, The Role of Eolian Processes in Forming Surface Features of the Martian Polar Layered Deposits, *Icarus*, 144, 267
- Hughes, T., 1975, A differential ablation-longitudinal compression mechanism for generating wave trains on cold alpine glaciers, *Proc. of the Moscow Symposium*, Aug. 1971, IAHS-AISH Publ. No. 104.
- Keller, H. U., Skorov, Yu. V., Markiewicz, W. J., Basilevsky, A. T., 2000, Stability of Water Ice Beneath Porous Dust Layers of the Martian South Polar Terrain, Mars Polar Science [Abstract]

- Kolb, E. J. & Tanaka, K. L., 2001, Geologic history of the polar regions of Mars based on Mars Global Surveyor data. II. Amazonian period. *Icarus*, 154, 22
- Kuti, A., 2009, Thermal Behavior of Dokka Crater and its Surroundings in the North Polar Region of Mars, LPSC XL [Abstract]
- Kuzmin, R. O., Greeley, R., Rafkin, S. C. R., & Haberle, R., 2001, Wind-Related Modification of Some Small Impact Craters on Mars, *Icarus* 153, 61
- Laskar, J., Levrard, B., & Mustard, J. F., 2002, Orbital forcing of the martian polar layered deposits, *Nature*, 419, 375
- Malin, M. C. & Edgett, K. S., 2001, Mars Global Surveyor Mars Orbiter Camera: Interplanetary cruise through primary mission, *J. Geophys. Res.*, 106, 23429
- Melosh, H. J., 1989, *Impact Cratering: A Geologic Process*, Oxford Monographs on Geology and Geophysics No. 11
- Neumann, G. A., Rowlands, D. D., Lemoine, F. G., Smith, D. E., & Zuber, M. T., 2001, Crossover analysis of Mars Orbiter Laser Altimeter data, *J. Geophys. Res.*, 106, 23753-23768
- Paige, D. A. & Keegan, K. D., 1994, Thermal and albedo mapping of the polar regions of Mars using Viking thermal mapper observations: 2. South polar region, *J. Geophys. Res.*, 99, 25993-26013
- Plaut, J. J., Picardi, G., Safaeinili, A., Ivanov, A. B., Milkovich, S. M., et al., 2007, Subsurface Radar Sounding of the South Polar Layered Deposits of Mars, *Science*, 316, 92-95
- Russell, P. S., Head, J. W., & Hecht, M. H., 2004, Evolution of ice deposits in the environment of Martian circumpolar craters and implications for polar cap history. LPSC XXXV, 1 [Abstract]

- Russell, P. S. & Head, J. W., 2005, Circum-polar Craters with Interior Deposits on Mars: Polar Region Geologic, Volatile, and Climate History with Implications for Ground Ice Signature in Arabia Terra, LPSC XXXVI, 1 [Abstract]
- Scott, D. H. & Carr, M. H., 1978, Atlas of Mars, I-1083, USGS
- Seu, R., Phillips, R. J., Biccari, D., et al., 2007. SHARAD sounding radar on the Mars Reconnaissance Orbiter. *J. Geophys. Res.*, 112, 1-18.
- Seu, R., Phillips, R. J., Biccari, D., et al., 2007. Accumulation and Erosion of Mars' South Polar Layered Deposits. *Science*. 317, 1715-1718.
- Smith, D. E., Zuber, M. T., Frey, H. V., Garvin, J. B., Head, J. W., et al., 2001, Mars Orbiter Laser Altimeter: Experiment Summary after the first year of global mapping of Mars, *J. Geophys. Res.*, 106, 23689-23722
- Supulver, K. D., Edgett, K. S., & Malin, M. C. 2001. Seasonal Changes in Frost Cover in the Martian South Polar Region: Mars Global Surveyor LPSC XXXII, 1 [abstract]
- Tanaka, K. L. & Kolb, E. J. 2001. Geologic History of the Polar Regions of Mars Based on Mars Global Surveyor Data. *Icarus*, 154, 3-21.
- Tanaka, K. L. & Scott, D., 1987, Geologic Map of the Polar Regions of Mars. U. S. Geol. Surv. Misc. Invest. Ser., Map I-1802-C
- Thomas, P. & C. Weitz 1989. Sand Dune Materials and Polar Layered Deposits on Mars. *Icarus*, 81, 185-215.
- Toigo, A. D., Richardson, M. I., Wilson, R. J., Wang, H., & Ingersoll, A. P., 2002, A first look at dust lifting and dust storms near the south pole of Mars with a mesoscale model, *J. Geophys. Res.*, 107, 4-1
- Toon, O. B., Pollack, J. B., Ward, W., Burns, J. A., & Bilski, K. 1980. The Astronomical Theory of Climatic Change on Mars. *Icarus*, 44, 552-607.

Watters, W. A. & Zuber, M. T., in preparation

Whiteman, C. D. Kring, D. A., & Hoch, S. W., 2008, Diurnal Evolution of Atmospheric Structure within Meteor Crater, Arizona: Implications for Microniches on Mars, LPSC XXXIX, Abstract #1391

Zuber, M. T., Smith, D. E., Solomon, S. C., Muhleman, D. O., Head, J. W., Garvin, J. B., Abshire, J. B., & Bufton, J. L., 1992, The Mars Observer laser altimeter investigation, J. Geophys. Res., 97, 7781-7797

Zuber, M. T., Phillips, R. J., Andrews-Hanna, J. C., Asmar, S. W., Konopliv, A. S., Lemoine, F. G., Plaut, J. J., Smith, D. E., Smrekar, S. E. 2007. Density of Mars' Solar Polar Layered Deposits. Science, 317, 1718-1719.